Reconstructing Upper-Ocean Vertical Velocity Field from Sea Surface Height in the Presence of Unbalanced Motion

BO QIU AND SHUIMING CHEN

Department of Oceanography, University of Hawai'i at Mānoa, Honolulu, Hawaii

PATRICE KLEIN, HECTOR TORRES, JINBO WANG, LEE-LUENG FU, AND DIMITRIS MENEMENLIS

Jet Propulsion Laboratory, California Institute of Technology, Pasadena, California

(Manuscript received 27 July 2019, in final form 17 October 2019)

ABSTRACT

Reconstructability of upper-ocean vertical velocity w and vorticity ζ fields from high-resolution sea surface height (SSH) data is explored using the global 1/48° horizontal-resolution MITgcm output in the context of the forthcoming Surface Water and Ocean Topography (SWOT) mission. By decomposing w with an omega equation of the primitive equation system and by taking into account the measurement design of the SWOT mission, this study seeks to reconstruct the subinertial, balanced w and ζ signals. By adopting the effective surface quasigeostrophic (eSQG) framework and applying to the Kuroshio Extension region of the North Pacific, we find that the target and reconstructed fields have a spatial correlation of ~0.7 below the mixed layer for w and 0.7–0.9 throughout the 1000-m upper ocean for ζ in the error-free scenario. By taking the SWOT sampling and measurement errors into account, the spatial correlation is found to decrease to 0.4–0.6 below the mixed layer for w and 0.6–0.7 for ζ, respectively. For both w and ζ reconstruction, the degradation due to the SWOT errors is more significant in the surface layer and for smaller-scale signals. The impact of errors lessens with the increasing depth and lengthening horizontal scales.

1. Introduction

Accumulation of high-precision nadir-looking satellite altimetry data of the past 27 years has significantly advanced our knowledge of the mesoscale ocean circulation variability with horizontal scales ranging from 200 to 800 km (see, e.g., recent comprehensive reviews by Fu et al. 2010; Morrow et al. 2017). In this spatial scale range, the oceanic variability is largely in geostrophic or cyclostrophic balance and it controls the upper-ocean horizontal kinetic energy level and distribution (Ferrari and Wunsch 2009). Indeed, by taking advantage of the multidecade altimetry record, many recent studies have investigated the characteristics of global mesoscale eddies and their impact on horizontal material/tracer transport (Chelton et al. 2011; Zhang et al. 2014; Dong et al. 2014; McGillicuddy 2016, and references cited therein).

In contrast to the 200–800-km mesoscale eddy variability that dictates the horizontal oceanic transport, the upper-ocean vertical transport of heat, salt, and tracers is dominated by shorter mesoscale and submesoscale variability in the O(1–200) km range. Within this range, the upper-ocean circulation is less constrained geostrophically and the resultant divergent/convergent flows can lead to enhanced vertical motions (Klein and Lapeyre 2009; McWilliams 2016). In addition to their contributions to the mixed layer evolution, air–sea interaction, and upper-ocean water mass transformation, the shorter mesoscale and submesoscale-induced vertical motions have been found to play critical roles in controlling the CO_2 uptake, nutrient supply, and biogeochemistry of the upper ocean (e.g., Lévy et al. 2012; Pascual et al. 2015; Mahadevan 2016).

Despite its importance, directly measuring the upper-ocean vertical circulation has proven challenging. A widely used indirect approach to diagnose the upper-ocean vertical velocity is to adopt the quasigeostrophic (QG) omega equation put forth originally to study the atmospheric frontogenesis (Hoskins et al. 1978). By measuring

Denotes content that is immediately available upon publication as open access.

Corresponding author: Bo Qiu, bo@soest.hawaii.edu

DOI: 10.1175/JPO-D-19-0172.1

the three-dimensional (3D) finescale density field, the upper-ocean vertical circulation was successfully quantified by Pollard and Regier (1992), Rudnick (1996), and others with the use of QG omega equation. In the oceanic context where the local Rossby number is not small, the QG omega equation has been extended by several recent studies to include ageostrophic processes that were neglected in the original QG framework (e.g., Pallàs Sanz and Viúdez 2005; Nagai et al. 2006; Giordani et al. 2006).

As the synoptic measurements of 3D density and horizontal flow field are expensive and necessarily confined in space, a new approach to infer the upper-ocean vertical velocity field derives from the theory of surface quasigeostrophy (SQG) (Blumen 1978; Held et al. 1995). In the SQG framework, the interior flow structures are determined solely by surface buoyancy condition. For its oceanic application, Lapeyre and Klein (2006) relaxed the zero interior potential vorticity (PV) assumption and proposed an effective SQG (eSQG) formalism in which the surface and interior PV anomalies are related by an effective upper-ocean buoyancy frequency that can be calculated from climatological observations.

The SQG and eSQG approaches have been used by many studies to reconstruct the upper-ocean 3D structures, including the vertical velocity field (e.g., LaCasce and Mahadevan 2006; Isern-Fontanet et al. 2006, 2008; Klein et al. 2009; Smith and Vanneste 2013). Recent advancement relating to the SQG reconstruction includes the addition of surface mixed layer mixing effect (Ponte et al. 2013), improved denoising techniques on input sea surface tempearture (SST) data (Isern-Fontanet and Hascoët 2014), and the use of both sea surface height (SSH) and SST to constrain simultaneously the surface and interior PV (Ponte and Klein 2013; Wang et al. 2013; Gonzalez-Haro and Isern-Fontanet 2014). For the present study, we choose to use the eSQG approach to explore the potential of SWOT SSH data for the upper-ocean reconstructions. The adoption of this approach, as will be detailed in sections 3 and 4, limits the reconstructed motions to be adiabatic and QG balanced.

Using the Ka-band radar interferometer (KaRIn) technique, the SWOT satellite mission is designed to produce a 120-km-wide swath of surface elevation measurements (https://swot.jpl.nasa.gov). Scheduled for launch in September 2021, SWOT is expected to capture, on a global average, the oceanic meso and submesoscale circulation features at spectral wavelength scales $\geq 15\,\mathrm{km}$[1] (Fu and Ubelmann 2014; Wang et al. 2018). By measuring the 2D SSH signals in this mesosubmesoscale range, the SWOT mission will likely bring about a fundamental change in how we detect and comprehend the upper-ocean vertical circulation and its dynamics active in the horizontal 15–200-km range.

To explore the potential of reconstructing the 3D upper-ocean circulation, including the vertical velocity field, from the SWOT SSH data, Qiu et al. (2016) have recently utilized the 1/30° submesoscale-permitting OGCM for Earth Simulator (OFES) model output (Sasaki et al. 2014) and subjected it through the SWOT simulator that generates the along-swath SSH data with expected measurement errors. By adopting the eSQG formalism and modeled SSH data as input, we compared the eSQG-reconstructed upper-ocean relative vorticity ($\zeta = \partial v/\partial x - \partial u/\partial y$) and vertical velocity w fields to the original model output in the Kuroshio Extension region. For the 1000-m upper ocean below the surface mixed layer, the correlation between the modeled and reconstructed ζ and w are 0.7–0.9 and 0.6–0.7, respectively. Degradation due to the SWOT sampling and measurement errors for the ζ and w reconstruction was found to be moderate: 5%–25% for ζ and 15%–35% for w.

One deficiency of the 1/30° OFES simulation is that it does not include tidal forcing. Over the 15–200-km wavelength range of our interest, many recent observational and modeling studies have pointed to the importance of unbalanced motions related to internal tides and inertial gravity waves in masking the SSH signals (Callies et al. 2015; Rocha et al. 2016a,b; Savage et al. 2017a,b; Qiu et al. 2017, 2018; Arbic et al. 2018; Torres et al. 2018). Because of the lack of tidal forcing, the 1/30° OFES simulation underestimates the energy level of unbalanced motion, making it more favorable in reconstructing the 3D upper-ocean circulation based on the expected SWOT SSH measurements alone.

To improve the assessment of reconstructing the upper-ocean circulation under the setting of realistic balanced versus unbalanced motions, we reexamine in this study the reconstructability issue by using output from the global 1/48° horizontal resolution Massachusetts Institute of Technology General Circulation Model (MITgcm) simulation that incorporates external tidal forcing. As will be detailed in section 2, the MITgcm simulation has a reasonable representation of kinetic energy level of the balanced/unbalanced motions of the World Ocean. Under the combined surface wind and tidal forcing, energetic vertical circulations of different origins emerge in the meso and submesoscale range of $O(10–200)$ km. In comparison to our 2016 study, a new

[1] The 15-km wavelength value is obtained under the assumption of 2-m significant wave height. See Wang et al. (2019) and Callies and Wu (2019) for seasonally and geographically dependent wavelength scales resolvable by SWOT in the World Ocean.

aspect of the present study is a careful diagnosis of the w signals with different dynamic origins. In the context of SWOT mission, we try to identify that part of the w signals that are retrievable from the SWOT-measured SSH data and are, at the same time, relevant for the vertical transfer of heat and materials in the upper ocean.

This paper is organized as follows. In section 2, we provide a brief description about the 1/48° MITgcm simulation and its performance in resolving the global balanced and unbalanced circulation variability. In section 3, the modeled vertical velocity signals are diagnozed and the relevant w signals are identified within the context of SWOT spatiotemporal measurement configurations. After briefly reviewing the eSQG framework in section 4, we apply it to reconstruct the 3D vertical velocity and relative vorticity field in the Kuroshio Extension region. Section 5 provides details about the SWOT simulator and our approach to generate the objectively mapped SSH field. With the use of the objectively mapped SSH field, we examine further in section 5 the reconstructability of the 3D upper-ocean circulation features and quantify the effect due to the SWOT sampling and measurement errors. Section 6 summarizes the findings from the present study and provides perspectives for future explorations.

2. MITgcm LLC4320 simulation

The model output analyzed in this study is based on the state-of-the-art global ocean simulation of MITgcm (Marshall et al. 1997) in a latitude–longitude–cap (LLC) configuration with a polar cap that has 4320 × 4320 grid cells. Referred to as LLC4320, the model has a 1/48° horizontal resolution and 90 vertical levels. To better resolve the submesoscale upper-ocean variability, the model's vertical levels have a ~1-m vertical resolution at the surface and increase to ~30 m near 500-m depth. The LLC4320 simulation is initialized from the output of the Estimating the Circulation and Climate of the Ocean, Phase II (ECCO2), project (Menemenlis et al. 2008), with the subsequent model resolution increased to LLC1080 (1/12°), LLC2160 (1/24°), and the present LLC4320 (1/48°). The LLC4320 model is forced by the 6-hourly, 0.16° horizontal resolution ECMWF atmospheric reanalysis, as well as by an equivalent surface pressure field consisting of the full lunar and solar tidal potential (Weis et al. 2008). For our analysis, we use the hourly snapshots of the modeled SSH η, potential temperature θ, salinity S, and velocity (u, v, w) data from 1 November 2011 to 31 October 2012 (366 days).

Several recent studies have attempted to verify the circulation changes modeled in the LLC4320 simulation. By comparing the global surface eddy kinetic energy (EKE) distribution derived from the AVISO SSH product and that simulated by LLC4320 averaged to the AVISO grid, Qiu et al. (2018) found that by and large, LLC4320 simulates faithfully the mesoscale eddy variability captured by the satellite altimeter missions that have spectral scales larger than $O(150)$ km. One exception occurs within the equatorial band of ±10°, where the AVISO-derived EKE values are consistently larger than those based on LLC4320. A reason for this discrepancy is likely related to the measurement errors in the AVISO SSH data that are amplified when converting to EKE due to the small Coriolis parameter within the equatorial band.

Comparisons between the LLC4320 simulation and repeat shipboard acoustic Doppler current meter (ADCP) measurements were conducted at different sites of the World Ocean. Across the Drake Passage, Rocha et al. (2016a) found a reasonable agreement between the modeled and observed along- and cross-track velocity structures. In the northwestern Pacific across the 137°E meridian, Wang et al. (2019) detected a good agreement between the simulated and observed zonal mean flow sturctures and Qiu et al. (2018) compared the LLC4320- and ADCP-derived transition scale L_t values, defined by the dominance from balanced to unbalanced motions. Both the ADCP and LLC4320 results reveal that $L_t = O(15)$ km in the Kuroshio region north of 28°N, $L_t = O(50)$ km in the Subtropical Countercurrent region of 14°–28°N, and $L_t > 200$ km in the North Equatorial Current region of 9°–14°N.

Evaluating the LLC4320's skill in simulating the unbalanced wave motions is challenging due to lack of in situ high-frequency SSH measurements in the World Ocean. By utilizing the hourly dynamic height time series from nine McLane profiler moorings available in the Pacific, North Atlantic, and South Indian Oceans, Savage et al. (2017b) found that the wave–frequency spectra of SSH variance simulated by LLC4320 agreed reasonably well with those observed by the profiler moorings. Although the LLC4320-simulated barotropic tides are ~10% overestimated relating to the tidal self-attraction and loading specification (B. Arbic 2019, personal communication), the recent study by Luecke et al. (2019, manuscript submitted to *J. Geophys. Res. Oceans*) found that LLC4320 simulated well in the internal gravity wave continuum when compared to the ~3000 available historical moored observations.

Given the available mesoscale eddy variability, ADCP-measured velocity, and high-frequency SSH comparisons summarized above, we believe the LLC4320 simulation provides an adequate dataset that allows us to reevaluate the reconstruction of upper-ocean circulation structures, including the vertical velocity,

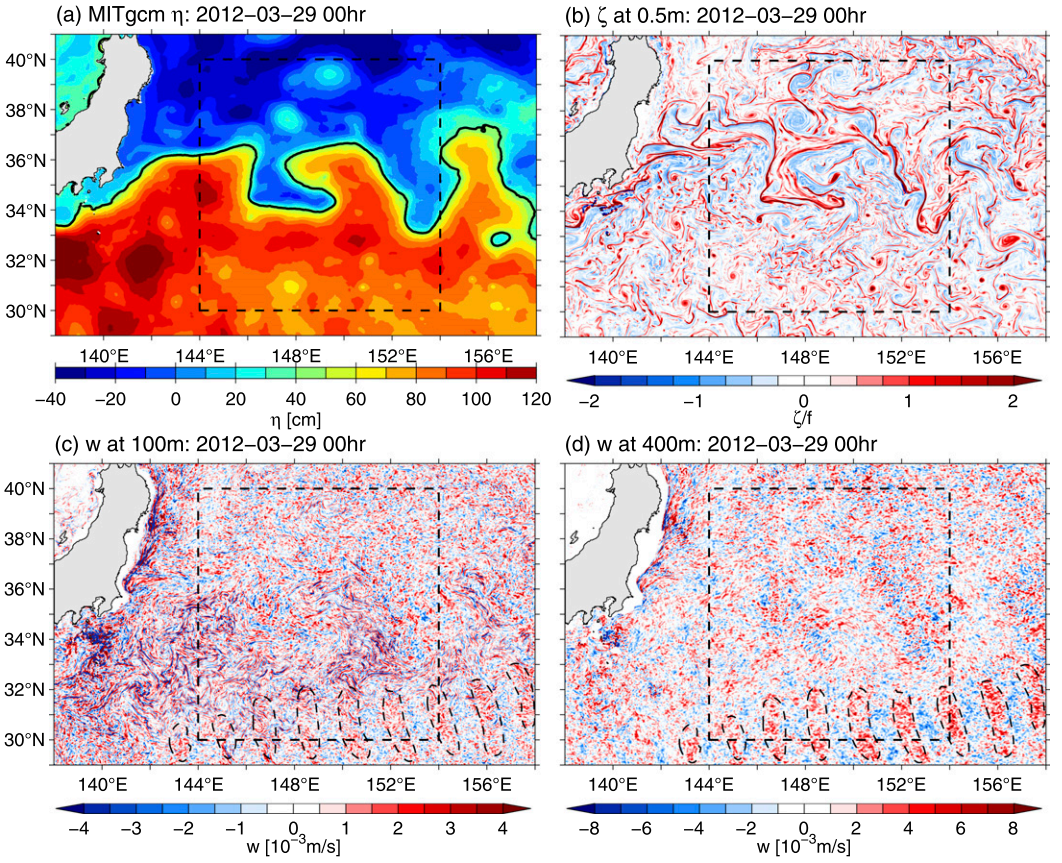

FIG. 1. Typical wintertime snapshot (a) sea surface height, (b) surface relative vorticity normalized by f, (c) vertical velocity at 100 m, and (d) vertical velocity at 400 m on 29 Mar 2012. The dashed box shows the region in which reconstruction of w and ζ is conducted. Notice that the scale for w is different in (c) and (d), and dashed contours in (c) and (d) indicate the internal tide–induced vertical velocity wave trains.

under a realistic setting of balanced versus unbalanced motions.

3. Vertical velocity in the context of SWOT measurements

Following our 2016 analysis, we will in this study explore the w field and its reconstruction in the Kuroshio Extension (KE) region east of Japan (Fig. 1). The region is representative of other western boundary currents in the World Ocean after they separate from the coastal boundary and enter the deep interior ocean (e.g., Imawaki et al. 2013). Figure 1 shows the typical wintertime snapshot SSH (Fig. 1a), surface relative vorticity ζ normalized by f (Fig. 1b), w at 100 m (Fig. 1c), and w at 400 m (Fig. 1d) fields from the LLC4320 simulation. The SSH map reveals that LLC4320 does a good job in simulating the separation of the KE jet at the observed latitude of 35°N and the presence of KE's quasi-stationary meanders and cutoff warm-/cold-core eddies. While it is not obvious in Fig. 1a, submesoscale features appear clearly in the surface ζ map: ubiquitous smaller-scale eddies with diameters < 50 km and elongated vorticity filaments with opposite signs can be seen in Fig. 1b. Notice that the simulated submesoscale eddies and filaments can have $|\zeta|/f$, or Rossby number, $>O(1)$. Similar features of surface ζ in the KE region have been reported in the 1/30° OFES simulation by Sasaki et al. (2014) and in the LLC4320 by Rocha et al. (2016a).

The instantaneous w maps shown in Figs. 1c and 1d exhibit dynamically different characteristics. At 100 m in the mixed layer, w shows laterally elongated features that are strained by the surface vorticity field (Fig. 1b). South of 33°N in Fig. 1c, one can clearly identify a sequence of wave trains that have a wavelength of ~175 km (cf. the dashed contours in Fig. 1c). A look at the sequential w maps indicates that these wave trains initiate from the meridionally oriented Izu–Ogasawara Ridge along 140°E and propagate eastward at a speed of 4.0 m s^{-1}. These characteristics suggest that these wave trains are the mode-1 M_2 internal tides generated by

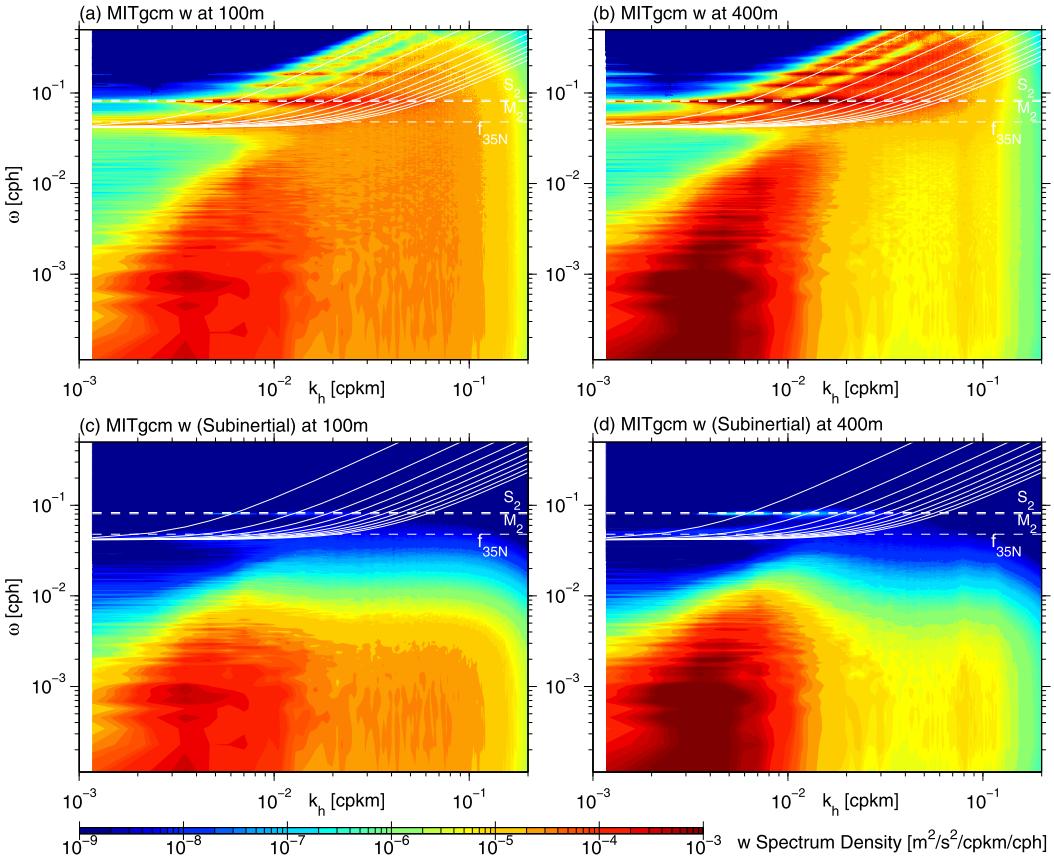

FIG. 2. Vertical velocity spectra as functions of horizontal wavenumber k_h and frequency ω for modeled w at (a) 100 m and (b) 400 m in the KE box 144°–154°E, 30°–40°N. (c),(d) As in (a) and (b), but for w after low-pass filtering by Eq. (1). Solid white lines denote the dispersion relation for inertia–gravity waves of the first 10 vertical modes. Dashed white lines denote the inertial frequency and S_2 and M_2 tidal frequencies.

barotropic M_2 tides interacting with the Izu–Ogasawara Ridge.[2] Indeed, a look at the horizontal wavenumber–wave frequency (k_h–ω) spectra of w at 100 m reveals that there exists a prominent spectral peak at the M_2 tidal frequency (Fig. 2a). After encountering the KE jet and its neighboring mesoscale eddy field north of 33°N, the M_2 internal tide wave trains are scattered and their spatial coherence disrupted. Notice that the laterally strained w signals of Fig. 1c show up spectrally in the broad submesoscale range of $k_h = 0.003$–0.1 cpkm in Fig. 2a.

The presence of the M_2 internal tide wave trains becomes more evident at the 400-m thermocline depth south of 33°N (Fig. 1d). As shown in the k_h–ω spectra of Fig. 2b, the M_2 internal tide variance at 400 m is in fact an order of magnitude larger than that at 100 m and this is dynamically understandable from the vertical structure of mode-1 internal waves (e.g., Gill 1982). In addition to the M_2 internal tide signals, Fig. 2b reveals that compared to 100-m depth, there exist much enhanced w signals in the superinertial frequency range at 400 m that satisfy the inertial gravity wave (IGW) dispersion relation of discrete vertical modes (denoted by the white curves in Fig. 2b). In the physical space, these IGW w signals appear as speckled patterns that are ubiquitous in Fig. 1d. Due to the use of instantaneous hourly model output, some of the simulated IGW w signals are aliased into the subinertial frequency band with $k_h =$ 0.05–0.15 cpkm in Fig. 2b. The aliasing problem due to the use of instantaneous hourly model output of LLC4320 has been noticed previously by Savage et al. (2017b) and Arbic et al. (2018). Although posing an issue in interpreting the spectral analysis results such as shown in Fig. 2, it has little impact on the reconstruction

[2] Based on the buoyancy frequency profiles $N(z)$, the mode-1 eigenvalue velocity has a value $c_1 = 3.14\,\mathrm{m\,s^{-1}}$ in the KE region. Given this c_1 value, the theoretical wavelength and phase speed of the mode-1 M_2 internal tides at 30°N are $L = 2\pi c_1/(\omega^2 - f^2)^{1/2} =$ 165 km and $c_p = \omega L/2\pi = 3.7\,\mathrm{m\,s^{-1}}$, respectively, where $\omega = 1.405 \times 10^{-4}\,\mathrm{s^{-1}}$ for M_2 tides and $f = 0.727 \times 10^{-4}\,\mathrm{s^{-1}}$ is the Coriolis parameter.

of upper-ocean circulation because the latter is based on the instantaneous SSH information of LLC4320.

a. Vertical velocity in the context of SWOT mission

While the vertical velocity signals in the KE region simulated by LLC4320 occupy a wide range in the k_h–ω space, not all these signals are relevant in the context of the SWOT measurements. Given that the eSQG framework is derived from the QG dynamics, it is reasonable to expect that the vertical velocity in the near- and superinertial bands may not be reconstructed from the SWOT-measured SSH data. Rather than the full w signals shown in Fig. 1 as the target w field for eSQG reconstruction, we will in this study use the low-pass-filtered w field:

$$w_{\rm lp}(x,y,z,t) = \sum_{t_i} w(x,y,z,t_i)\exp(-|t_i - t|/L_t)\,, \qquad (1)$$

as our target, where $L_t = 1.2$ days. Figures 2c and 2d show the $w_{\rm lp}$ spectra in the k_h–ω space. By construction, high-frequency w signals with $\omega > 0.01$ cph are significantly damped in the target $w_{\rm lp}$ field. For visual contrast between the original w and $w_{\rm lp}$ fields, we plot in Figs. 3a and 3g the $w_{\rm lp}$ maps at 100- and 400-m depths at the time of those for Figs. 1c and 1d (inside the dashed $10^\circ \times 10^\circ$ box). At 100 m in the mixed layer, Fig. 3a shows that while the wave trains associated with the M_2 internal tides are filtered out, many of the elongated submesoscale w signals seen in Fig. 1c remain discernible. These elongated w signals, as we noted above, are generated by mesoscale strain field that has scales longer than the inertial period. The difference between the instantaneous w and $w_{\rm lp}$ field becomes more stark at the 400-m depth of the main thermocline. While the w map in Fig. 1d is overwhelmed by the IGW signals with an amplitude of $O(10^{-2})$ m s^{-1}, Fig. 3g reveals that much of the $w_{\rm lp}$ is dominated by mesoscale features with an amplitude of $O(0.5 \times 10^{-3})$ m s^{-1}. In the following analyses, we will consider the $w_{\rm lp}$ signals exclusively in regard to the eSQG reconstruction. Furthermore, we will omit the subscript lp and simplify $w_{\rm lp}$ to w for brevity.

b. Diagnosis of vertical velocity field

By generalizing the **Q**-vector form of the QG omega equation of Hoskins et al. (1978) to include all other ageostrophic processes, Giordani et al. (2006) show that the 3D vertical velocity ω in the primitive equation oceanic system can be inverted from:

$$f^2\frac{\partial^2 \omega}{\partial z^2} + \nabla_h(N^2 \cdot \nabla_h \omega) = \nabla_h \cdot \mathbf{Q}, \qquad (2)$$

where $N^2 = -(g/\rho_0)\partial p/\partial z$ is squared buoyancy frequency, ∇_h is the horizontal gradient operator, and the **Q** vector is composed of contributions from six physical processes:

$$\mathbf{Q} = \mathbf{Q}_{\rm th} + \mathbf{Q}_{\rm dm} + \mathbf{Q}_{\rm tg} + \mathbf{Q}_{\rm tag} + \mathbf{Q}_{\rm dag} + \mathbf{Q}_{\rm dr}\,, \qquad (3)$$

where $\mathbf{Q}_{\rm th}$ denotes the turbulent buoyancy forcing, $\mathbf{Q}_{\rm dm}$ the turbulent momentum forcing, $\mathbf{Q}_{\rm tg}$ the geostrophic kinematic deformation, $\mathbf{Q}_{\rm tag}$ the ageostrophic kinematic deformation, $\mathbf{Q}_{\rm dag}$ the thermal wind imbalance deformation, and $\mathbf{Q}_{\rm dr}$ the material derivative of the thermal wind imbalance (TWI); see appendix A for detailed expressions and processes related to each **Q** component in Eq. (3). Since Eq. (2) is linear, we can invert ω from each component of the **Q** forcing separately. In the following, we will denote ω from the forcing $\mathbf{Q}_a$ as ω_a. Given the hourly LLC4320 output, contributions to ω from the $\mathbf{Q}_{\rm tg}$, $\mathbf{Q}_{\rm tag}$, $\mathbf{Q}_{\rm dag}$, and $\mathbf{Q}_{\rm dr}$ forcing can be evaluated by Eqs. (A8)–(A11) based on the procedures described in appendix A. Lack of the model information about the turbulent buoyancy and momentum mixing, however, prevents us from evaluating $\omega_{\rm th}$ and $\omega_{\rm dm}$ directly. In this study, we estimate $\omega_{\rm th} + \omega_{\rm dm}$ as the residual between the modeled w and ω forced by $\mathbf{Q}_{\rm tg} + \mathbf{Q}_{\rm tag} + \mathbf{Q}_{\rm dag} + \mathbf{Q}_{\rm dr}$ and denote it below as $\omega_{\rm mix}$.

Figures 3b–e show the ω signals inverted from the $\mathbf{Q}_{\rm tg}$, $\mathbf{Q}_{\rm tag}$, $\mathbf{Q}_{\rm dag}$, and $\mathbf{Q}_{\rm dr}$ forcing, respectively, at 100 m for 29 March 2012. The residual $\omega_{\rm mix}$ field is shown in Fig. 3f. Similar to the w map shown in Fig. 3a, all the ω signals have been low-pass filtered using Eq. (1). Visually, $\omega_{\rm tg}$ bears a good resemblance to w when finescale, IGW-related, speckled signals are removed. This is dynamically to be expected because $\mathbf{Q}_{\rm tg}$ works to generate the balanced vertical circulation. The spatial correlation between Figs. 3a and 3b is $r = 0.35$. The ω signal produced by $\mathbf{Q}_{\rm tag}$ also shows some correspondence to w; it, however, generates ω signals with spatial scales finer than those of $\omega_{\rm tg}$. The spatial correlation between Figs. 3a and 3c is $r = 0.28$. The TWI-induced $\omega_{\rm dag}$ and $\omega_{\rm dr}$ in Figs. 3d and 3e show similar spatial patterns and they appear mostly along the convoluted path of the KE jet (recall Fig. 1a). The spatial correlation between the w and $\omega_{\rm dag}$ ($\omega_{\rm dr}$) signals is $r = 0.05$ ($r = 0.29$). At this 100-m depth in the winter mixed layer, the turbulent forcing–induced $\omega_{\rm mix}$ is as important as the kinematic deformation forcing. The spatial correlation coefficient between w and $\omega_{\rm mix}$ in Figs. 3a and 3f reaches $r = 0.80$. The fact that the turbulent mixing controls the vertical circulation inside the mixed layer has been emphasized by Ponte et al. (2013) based on idealized high-resolution OGCM experiments with and without the presence of surface mixed layer.

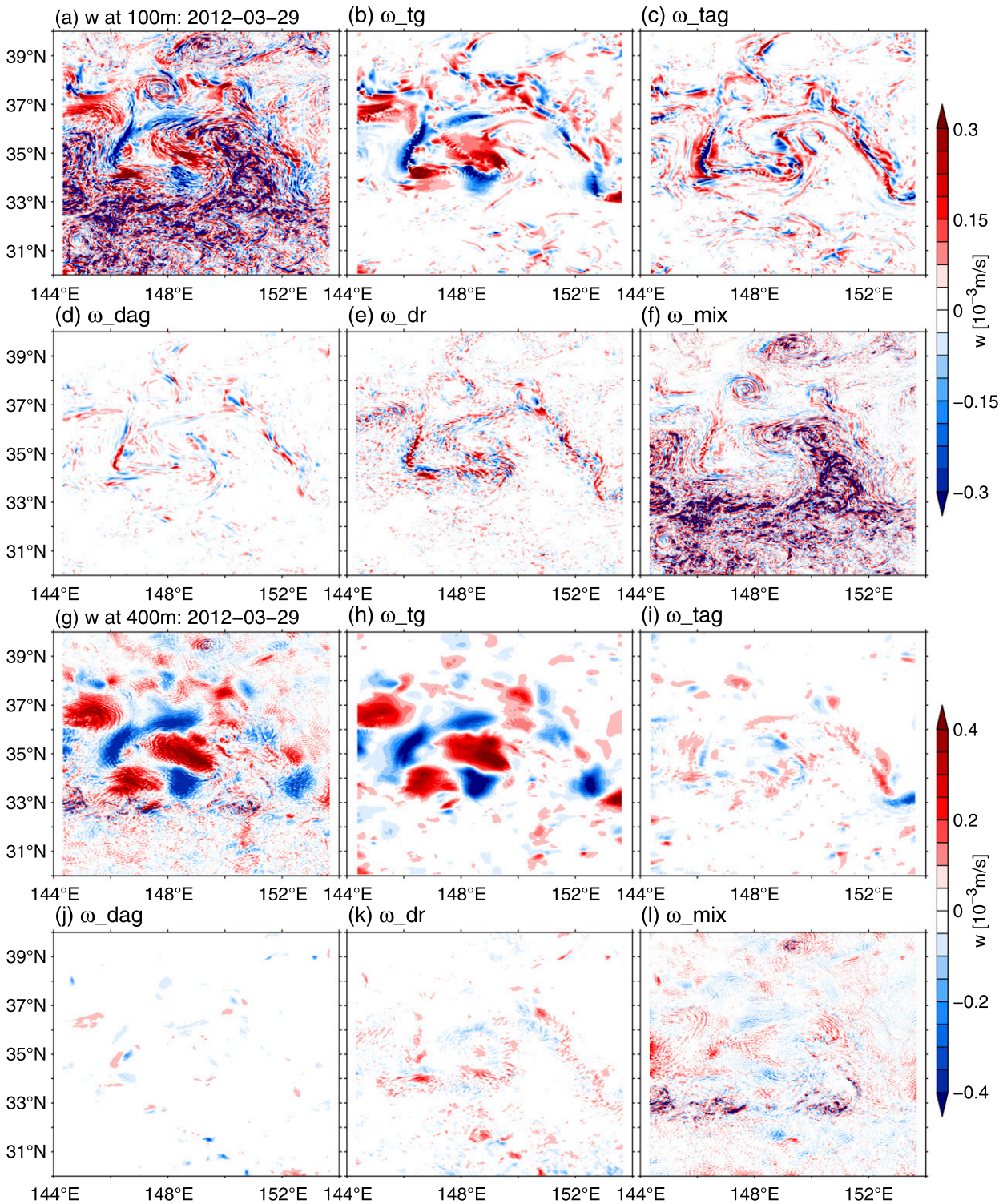

FIG. 3. Typical wintertime low-pass filtered (a) vertical velocity from LLC4320 and (b)–(f) its components from the ω Eq. (2) at 100-m depth, centered on 29 Mar 2012. (g)–(l) As in (a)–(f), but at 400-m depth.

Decomposition of w into the five ω components reveals a different character at the 400-m thermocline depth. As shown in Figs. 3g and 3h, most of the w signals at this depth are captured by ω_{tg} forced by the geostrophic kinematic deformation; the spatial correlation coefficient between ω_{tw} and the w field can reach up to $r = 0.84$. The ageostrophic kinematic deformation and TWI induced ω in Figs. 3i–k all show an insignificant contribution to the mesoscale w field. The turbulent mixing induced ω_{mix}, on the other hand, can be seen in Fig. 3l to control the small-scale w signals.

To contrast to the vertical velocity and ω features in winter, we present in Fig. 4 the summer example on 3 October 2012 of the low-pass-filtered w field and its decomposition into the five ω components. As demonstrated by many previous studies on seasonal differences in upper-ocean submesoscale variability (e.g., Mensa et al. 2013; Sasaki et al. 2014; Qiu et al. 2014), finescale vertical velocities induced by mixed layer instability are reduced significantly in summer. In contrast to Fig. 3a, the summer map of Fig. 4a reveals that w at 100-m depth is dominated by mesoscale features. A look at Fig. 4g indicates that these mesoscale w signals are, by and large, vertically coherent and that their magnitude amplifies with the increasing depth. Due to this dominance by mesoscales, it is not surprising to see that much of the w variance at both 100- and 400-m depths is captured by ω_{tg} forced by the geostrophic kinematic deformation ($r = 0.85$ between Figs. 4a,b and $r = 0.91$ between Figs. 4g,h). Contributions from all other ω components to w are minor.

To generalize the results shown in Figs. 3 and 4, we plot in Fig. 5 (left column) the spatial correlation coefficient r between w and the five ω components as a function of depth and time. The r values averaged over the full year of LLC4320 output is shown in the right column of Fig. 5. Consistent with what we have found above, the w signals are mostly determined by the ω_{tg} component forced by the geostrophic kinematic deformation. The exception occurs within the mixed layer (denoted by the black curve in Fig. 5a) where ω_{tg} explains only the balanced part of the modeled w signals. The remaining w signals within the surface mixed layer are explained by the ω_{mix} component induced by the turbulent buoyancy/momentum mixing (Fig. 5i) and, to a lesser extent, by ω_{tag} induced by the ageostrophic kinematic deformation (Fig. 5b). The TWI-induced ω_{dag} and ω_{dr}, as shown in Figs. 5c and 5d, both make minor contributions to w.

Given the major roles played by ω_{tg}, we will use it below as our target vertical velocity for reconstruction within the eSQG framework. Dynamically, this is equivalent to the task that we seek to reconstruct the w signals that are induced by balanced motions of the upper-ocean circulation. For consistency with the Qiu et al. (2016) study, reconstructability of the relative vorticity ζ field will also be quantified.

4. Reconstruction based on LLC4320 output

To better understand the impact of sampling and measurement errors embedded in the SWOT mission, it is beneficial to assess first how well the upper-ocean w and ζ fields can be reconstructed through the eSQG dynamics given the "full" SSH information from LLC4320. As detailed in Lapeyre and Klein (2006), the eSQG theory assumes that the PV anomalies in the interior ocean are correlated to the surface PV (or surface buoyancy) anomalies. Under this assumption, the anomalous geostrophic streamfunction ψ at depth z becomes functionally related to the SSH η anomalies via

$$\hat{\psi}(\mathbf{k}, z) = \frac{g}{f_o}\hat{\eta}(\mathbf{k})\exp\left(\frac{N_o}{f_o}k_h z\right), \tag{4}$$

where the caret $\hat{}$ denotes the horizontal Fourier transform, $\mathbf{k} = (k_x, k_y)$ is the horizontal wavenumber vector, $k_h = |\mathbf{k}|$, f_o is the Coriolis parameter at a reference latitude (35°N here), g is the gravity constant, and N_o is an "effective" buoyancy frequency that takes into account contributions of the nonzero interior PV signals. Dynamically, Eq. (4) implies that the surface and interior dynamical quantities are related and that their relationship is wavenumber dependent. Once ψ is specified, relative vorticity, buoyancy, and vertical velocity in the upper ocean can be deduced through geostrophy, hydrostasy, and the advective buoyancy equation, respectively:

$$\hat{\zeta}(\mathbf{k}, z) = -k_h^2\hat{\psi}(\mathbf{k}, z), \tag{5}$$

$$\hat{b}(\mathbf{k}, z) = \frac{N_o k_h}{C}\hat{\psi}(\mathbf{k}, z), \quad \text{and} \tag{6}$$

$$\hat{w}(\mathbf{k}, z) = -\frac{C^2}{N_o^2}\left[-\widehat{J(\psi_s, b_s)}\exp\left(\frac{N_o}{f_o}k_h z\right) + \widehat{J(\psi, b)}\right], \tag{7}$$

where J is the Jacobian operator and subscript s denotes the surface value. For the two constants N_o and C in Eqs. (6) and (7), we set $N_o/f_o = 80$ so that N_o represents the 0–300-m mean upper-ocean buoyancy frequency value in the KE region of our interest (30°–40°N, 144°–154°E). In accordance with Klein et al. (2009), $C = 2.4$ is chosen such that the rms amplitude of reconstructed w matches that of the target ω_{tw} signals. For applications during the SWOT mission, the box-mean N_o value can be estimated by in situ temperature–salinity

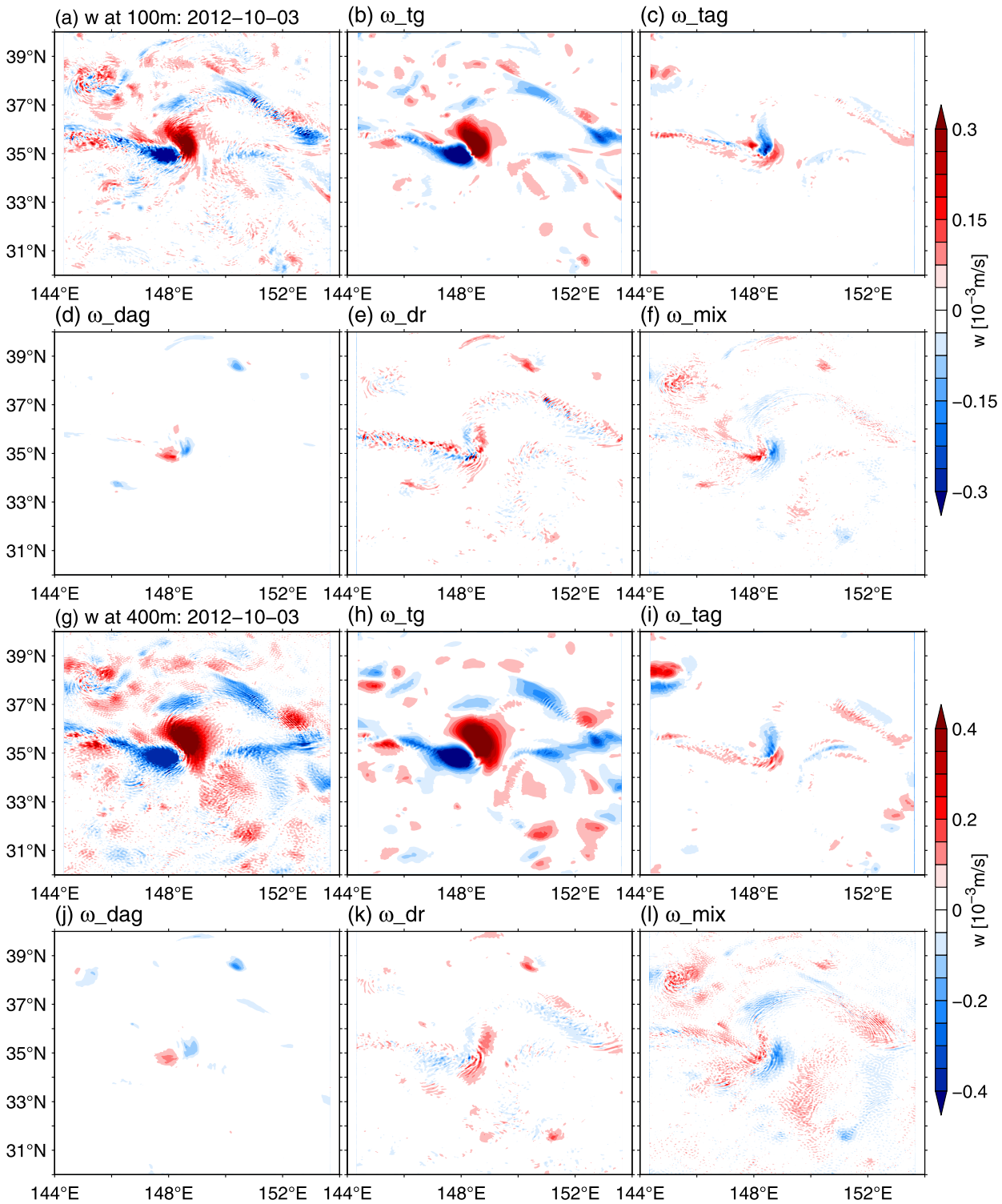

FIG. 4. Typical summertime low-pass filtered (a) vertical velocity from LLC4320 and (b)–(f) its components from the ω Eq. (2) at 100-m depth, centered on 3 Oct 2012. (g)–(l) As in (a)–(f), but at 400-m depth.

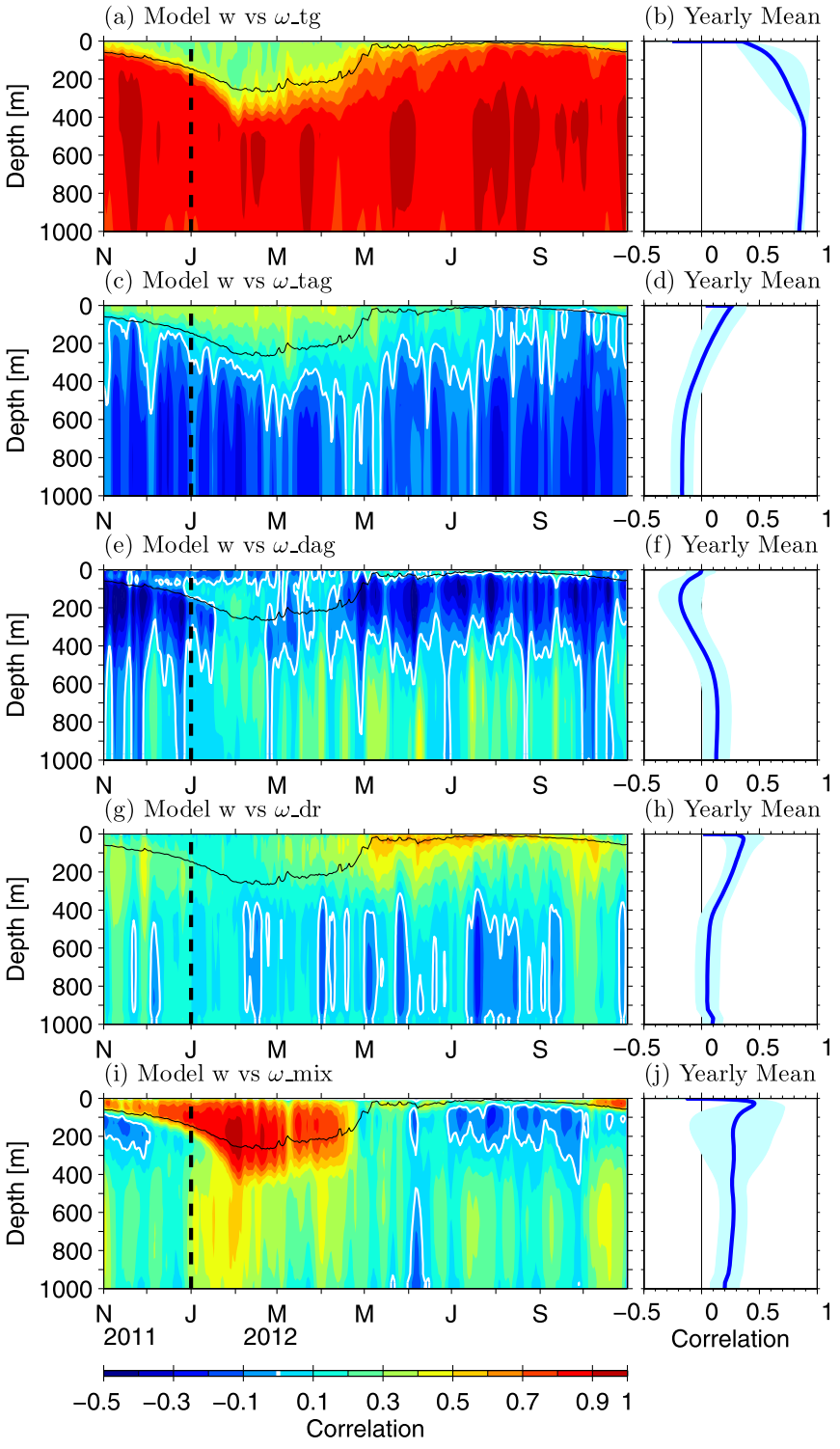

FIG. 5. Correlation as a function of time and depth between the low-pass filtered model w and (a) ω_{tg}, (c) ω_{tag}, (e) ω_{dag}, (g) ω_{dr}, and (i) ω_{mix} from the ω Eq. (2). Black lines denote the box-averaged mixed layer depth. (b),(d),(f),(h),(j) The yearly averaged correlation values as a function of depth for each ω component. Shaded areas denote the one standard deviation envelopes.

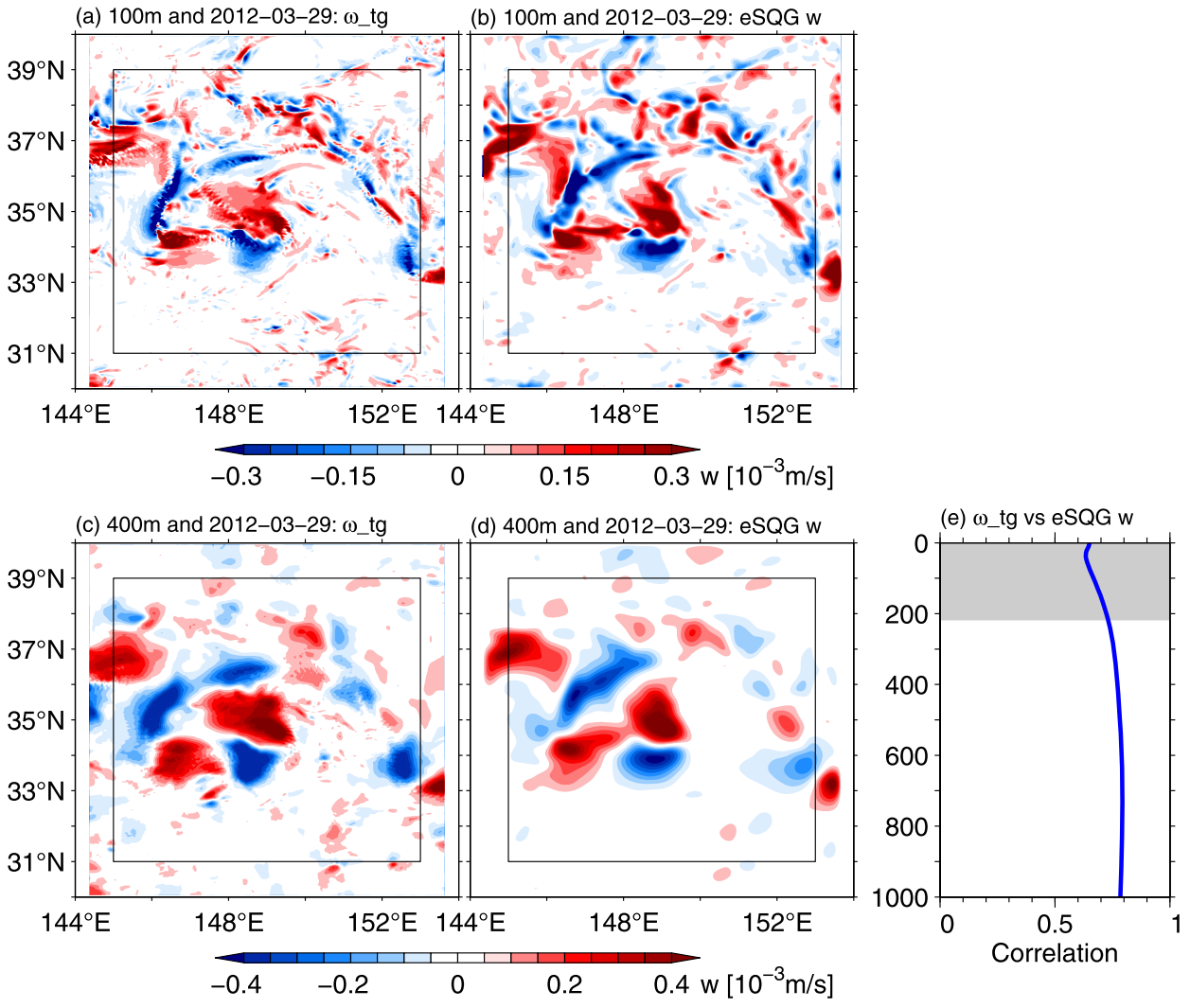

FIG. 6. Target vertical velocity field at (a) 100 and (c) 400 m for the wintertime example centered on 29 Mar 2012. The eSQG-reconstructed w field at (b) 100 and (d) 400 m. (e) Correlation between the target and reconstructed w as a function of depth. Gray shading denotes the domain-averaged mixed layer depth.

data from Argo floats. With respect to the C value upon which the amplitude of the eSQG-reconstructed w depends, it can be evaluated by concurrently measured SSH and surface buoyancy data through $C = (gN_o k_h/f_o)\,\hat{\eta}(\mathbf{k})/\hat{b}(\mathbf{k}, 0)$ from Eqs. (4) and (6).

To apply the eSQG reconstruction in the KE region, we use the LLC4320 SSH data $\eta(x, y, t)$ in the 30°–40°N and 144°–154°E box as input. To derive the $\hat{\psi}(\mathbf{k}, z)$ field in Eq. (4), we first low-pass filter the SSH data in time using Eq. (1), remove the large-scale SSH signals through the bilinear least-squared fitting, and then periodize the SSH field by doubling the $10° \times 10°$ box using mirror symmetry in the x and y directions. Once $\hat{\eta}(\mathbf{k})$ is obtained by Fourier transform, the 3D vorticity and vertical velocity fields are reconstructed through Eqs. (5) and (7) via the inverse Fourier transform. To avoid the edge effect, our comparison below between the target and reconstructed fields will be conducted in the 31°–39°N and 145°–153°E box of our initial selection.

Figures 6a and 6b compare the target ω_{tg} field and the reconstructed w field from Eq. (7) at the 100-m depth centered on 29 March 2012. The reconstructed w captures most of the mesoscale w_{tg} signals, but fail to recover features with spatial scales $< O(50)$ km. As a result, the spatial correlation coefficient between Figs. 6a and 6b is modest at $r = 0.66$ (Fig. 6e). Due to the weakening of submesoscale w_{tg} signals below the mixed layer, a comparison between Figs. 6c and 6d indicates that the reconstructed w at 400-m depth is capable of capturing most of the target ω_{tg} signals with

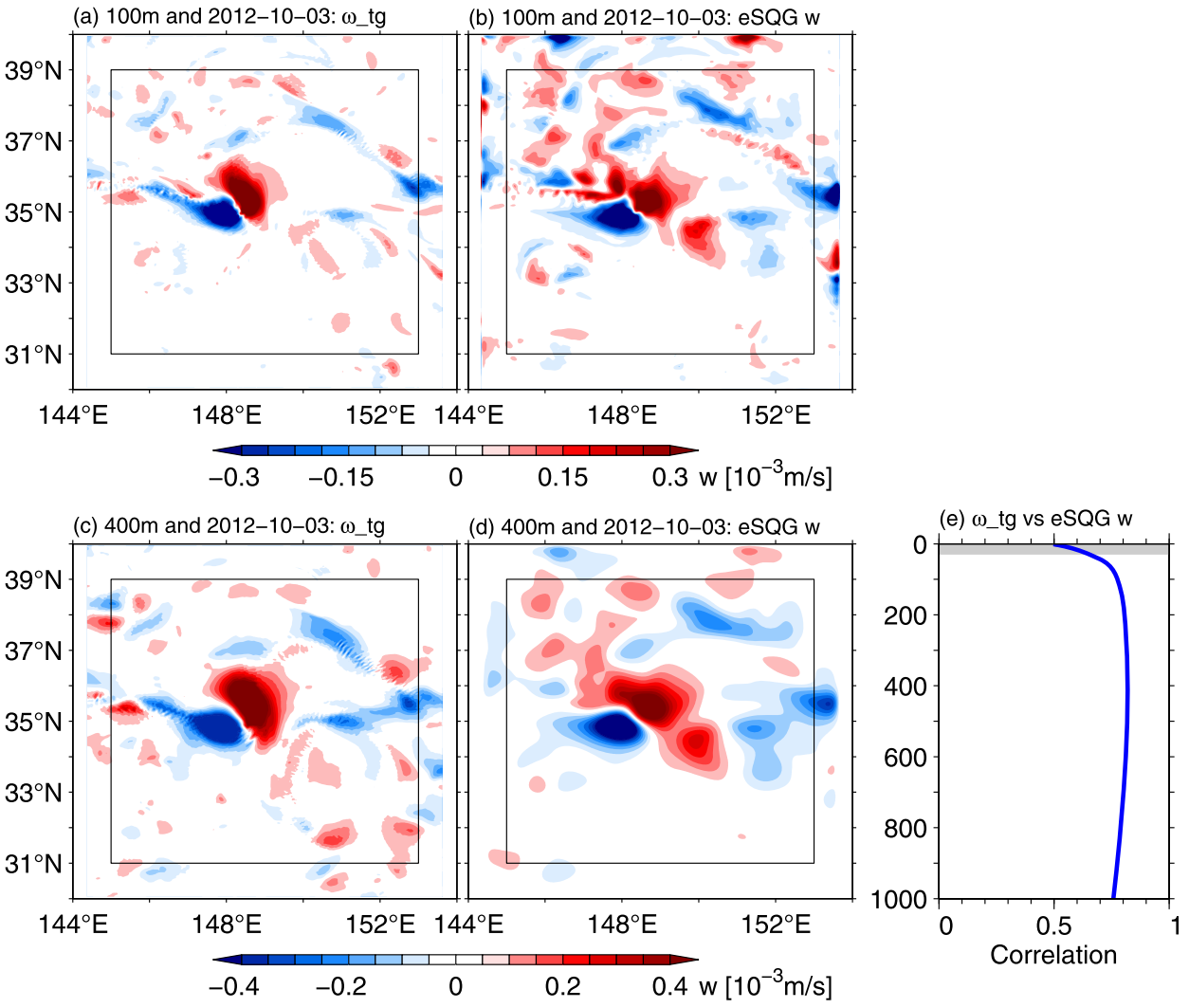

FIG. 7. Target vertical velocity field at (a) 100 and (c) 400 m for the summertime example centered on 3 Oct 2012. The eSQG-reconstructed w field at (b) 100 and (d) 400 m. (e) Correlation between the target and reconstructed w as a function of depth. Gray shading denotes the domain-averaged mixed layer depth.

r reaching 0.78. As shown in Fig. 6e, this contrast between the results at 100- versus 400-m depth is representative of the overall reconstruction results for w within and below the winter mixed layer. This feature, with r improving with an increasing depth, can also be found in the previous studies of the eSQG-based w reconstruction (e.g., Klein et al. 2009; Isern-Fontanet and Hascoët 2014).

In comparison to the winter results presented in Fig. 6, the summer reconstruction results for vertical velocity exhibit similar characteristics with respect to the contrast across the base of the mixed layer (Fig. 7). Because of the overall reduction in submesoscale upper-ocean turbulence in summer, the spatial correlation between the target and reconstructed w fields is comparable to that of the winter case below the mixed layer. As shown in Fig. 7e, for example, the r value reaches in general to 0.8 below the shallow summer mixed layer.

For completeness, we compare in Figs. 8a–c the winter surface ζ field from the LLC4320 simulation and that from the eSQG reconstruction Eq. (5) for 29 March 2012. Unlike the vertical velocity reconstruction shown in Fig. 6, in addition to mesoscales, even the submesoscale surface ζ signals are by and large captured by the eSQG reconstruction. The spatial correlation coefficient between Figs. 8a and 8b reaches to 0.83. Although deteriorating gradually with an increasing depth, Fig. 8c shows that the eSQG-reconstructed ζ matches the modeled ζ field well with $r > 0.7$ throughout the upper 800-m layer in this winter example case. As shown in

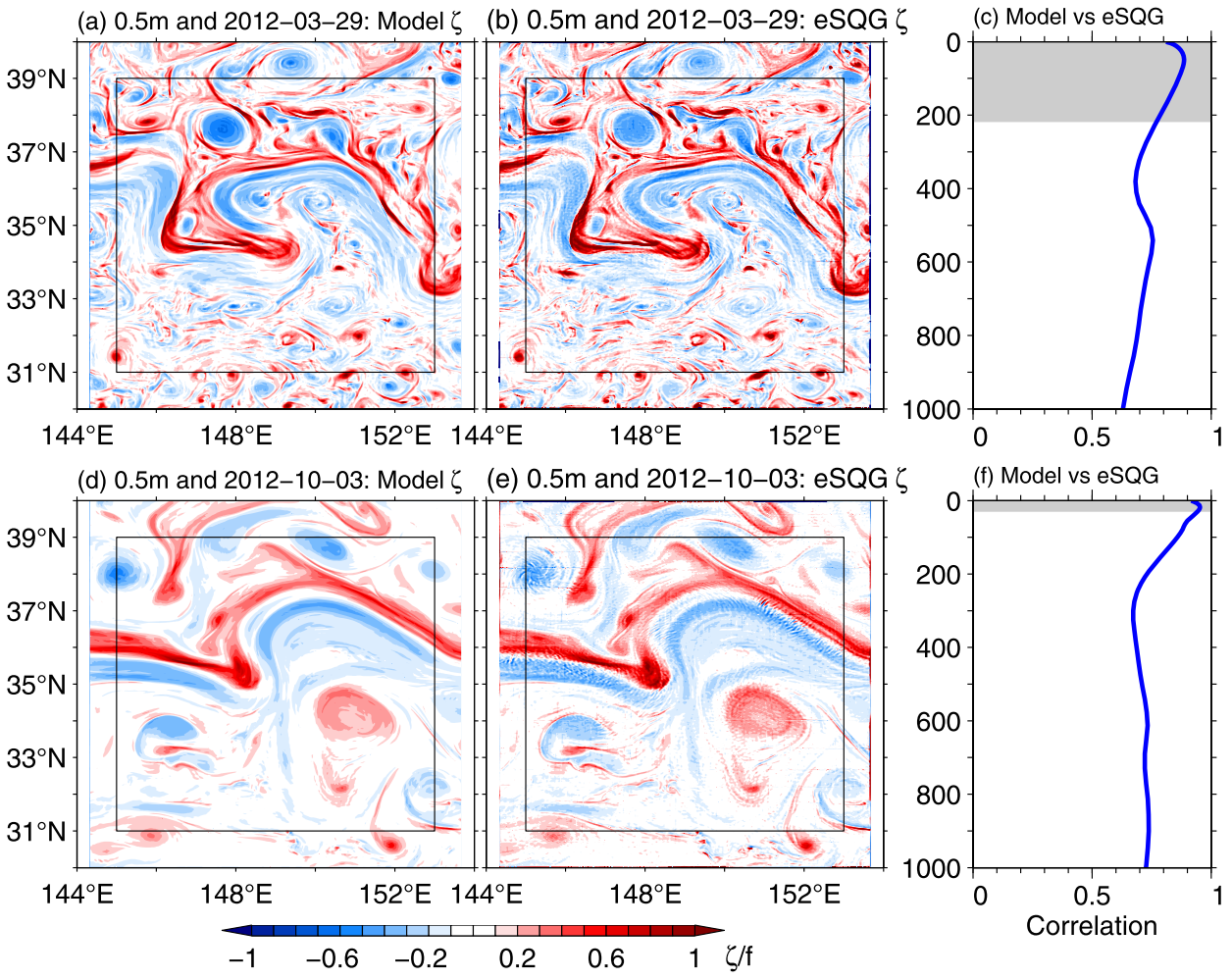

FIG. 8. (a) Target and (b) reconstructed near-surface relative vorticity field for the wintertime example centered on 29 Mar 2012. (c) Correlation between the target and reconstructed ζ as a function of depth. (d)–(e) As in (a)–(c), but for the summertime example centered on 3 Oct 2012. Gray shading in (c) and (f) denotes the domain-averaged mixed layer depth.

Figs. 8d–f, very similar spatial correlation results are obtained for the modeled versus reconstructed ζ fields in the summer example of 3 October 2012. Due to the reduction in submesoscale variance in the mixed layer, the r value can exceed 0.9 in the 50-m surface layer. Like the winter case, the r value decreases gradually to ~0.7 below the 200-m depth.

The winter and summer examples shown in Figs. 6–8 are typical of the w and ζ reconstructions obtained throughout the yearlong LLC4320 simulation in the Kuroshio Extension region. In Fig. 9, we summarize the spatial correlations between the target and reconstructed w and ζ fields as a function of time and depth. Averaged over the year, spatial correlation for w is generally low with $r \simeq 0.65$ in the upper 100-m layer (Fig. 9c). This low correlation is due to the low reconstructability of ω_{tg} in the seasonally varying surface mixed layer within which the eSQG dynamics fails to capture ω_{tg} signals with spatial scales shorter than $O(50)$ km. Below the surface mixed layer, the eSQG-reconstructed w has on average a correlation with the target ω_{tg} field at $r \simeq 0.7$. Notice that below the mixed layer, the r value shown in Fig. 9a is largely vertically uniform, but it can fluctuate between 0.5 and 0.9 on the intraseasonal time scales. A closer look at the LLC4320 output reveals that this time-varying r signal follows the rms fluctuations of the target ω_{tg} field (figure not shown): a more vigorous ω_{tg} field provides a better signal-to-noise ratio, leading to a more favorable reconstruction for w.

Additional insight into the w reconstruction can be gleaned by evaluating the correlations as a function of horizontal wavenumber k_h. As shown in Fig. 9b, for a fixed k_h, the correlation for w decreases monotonically with increasing depth; in other words, the eSQG

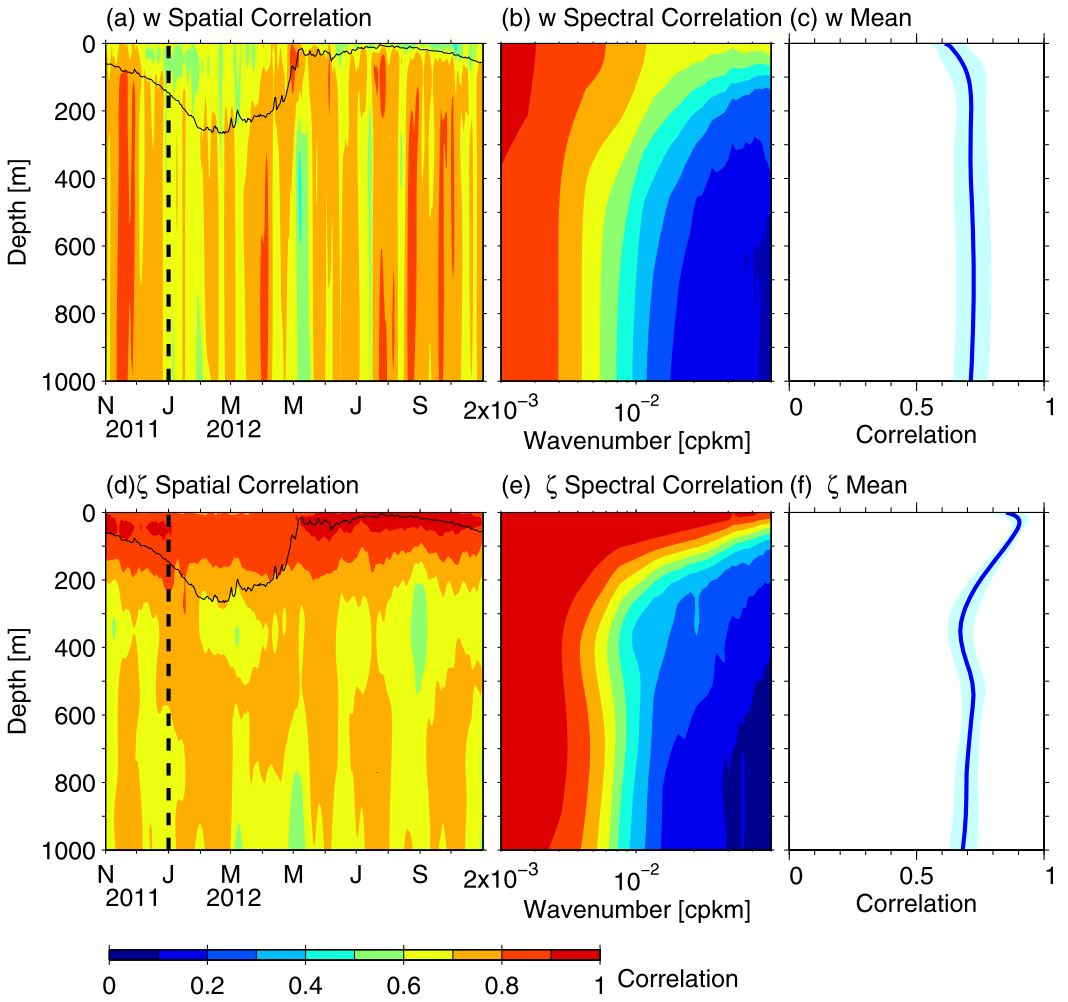

FIG. 9. (a) Correlation between the target and reconstructed w field as a function of depth and time. The black line denotes the time series of the domain-averaged mixed layer depth. (b) The same correlation as a function of horizontal wavenumber. (c) Yearly averaged correlation as a function of depth. (d)–(f) As in (a)–(c), but for the correlation between the target and reconstructed ζ field.

reconstruction for w is always better at a shallower depth than at a deeper layer. This result is somewhat counterintuitive in light of the average r profile in Fig. 9c that shows a better r value at depth. This counterintuitive result can be reconciled if we recall that the target w signal near the surface resides mostly in small wavelength range where r is low, whereas the target w signal has larger spatial scales in the deeper ocean where r is large.

For ζ reconstruction, the presence of the seasonally varying mixed layer poses no adverse impact (Fig. 9d). The annually averaged correlation coefficient between the target and reconstructed ζ generally exceeds $r = 0.85$ in the surface 100-m layer and falls to 0.7 in the thermocline layer below the 200-m depth (Fig. 9f). Compared to the w correlations shown in Fig. 9b, the k_h-dependent correlations for ζ is uniformly high in the surface layer with $r > 0.9$ over the entire k_h range (Fig. 9e); as a result, even though the surface ocean ζ is dominated by smaller-scale signals when compared to the deeper layer, the overall ζ reconstruction remains more favorable in the surface ocean than below.

5. Reconstruction with the use of SWOT simulator

In the preceding section, we have quantified the eSQG reconstruction of the upper-ocean w and ζ fields based on the full knowledge of the LLC4320 SSH output. When this approach is applied to the high-resolution SSH data from SWOT, considerations about the SWOT's time-dependent swath patterns and measurement errors have to be taken into account. To do so, we adopt the SWOT simulator that is designed to generate the synthetic SSH data along the SWOT ground swaths and add the

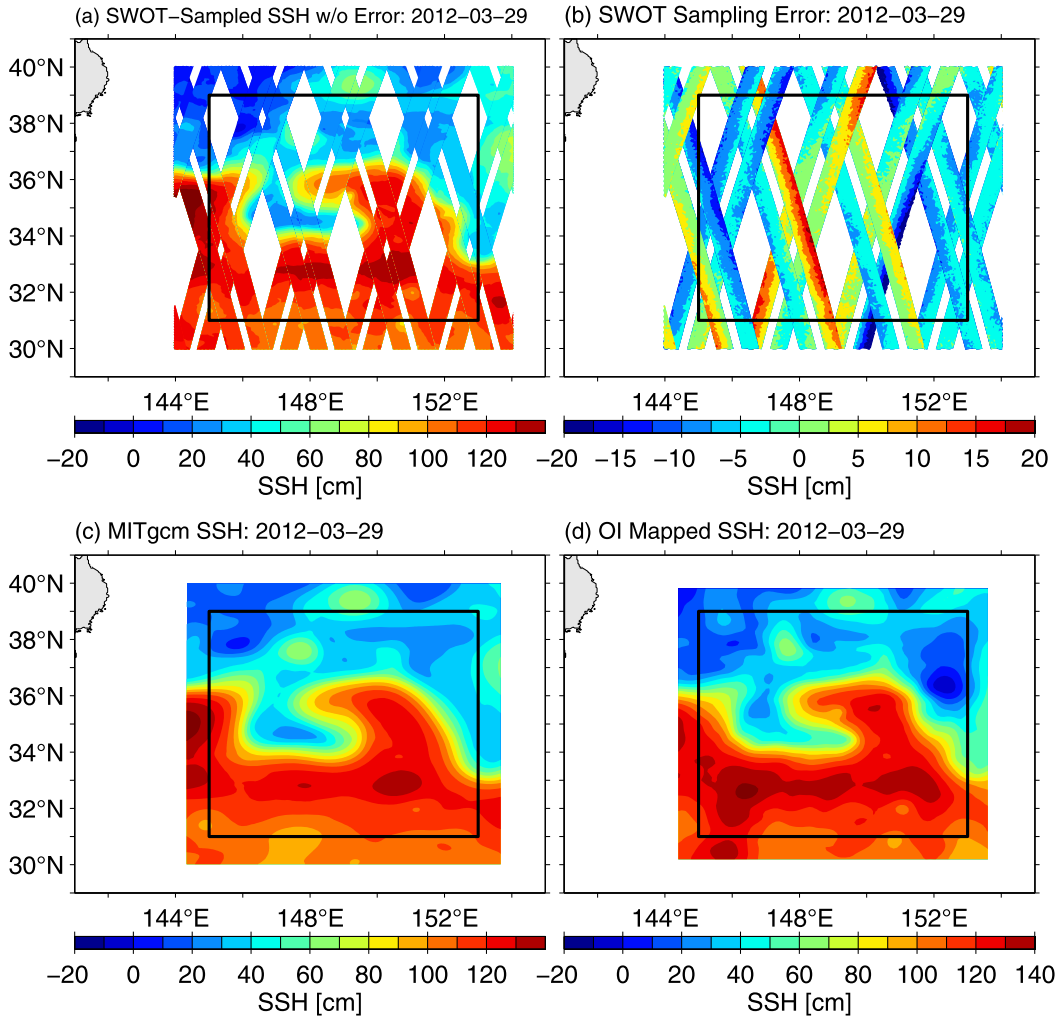

FIG. 10. (a) Along-swath SSH signals within the subcycle centered on 29 Mar 2012 generated by the SWOT simulator based on the hourly LLC4320 output. (b) SWOT simulator-generated along-swath SSH measurement errors. Note that the color scale for (b) is different from that in (a). (c) LLC4320 SSH map on 29 Mar 2012 after low-pass filtering by Eq. (1). (d) Objectively mapped SSH field on 29 Mar 2012 from the SSH input of (a) + (b).

measurement errors according to specifications by the SWOT project team (Gaultier et al. 2016; https://github.com/SWOTsimulator). The SWOT ground tracks in the 10° × 10° KE box of our interest are composed of ascending and descending swaths within a subcycle of ±3 days. Figure 10a shows the example of along-swath SSH signals generated by the SWOT simulator in the subcycle centered on 29 March 2012. Here, the SSH signals are based on the hourly SSH output of LLC4320 and the SSH discontinuities visible along the interleaving swath edges are because of the difference in satellite overpass timing. In Fig. 10b, we plot the SWOT simulator-generated SSH measurement errors, which have all spatial scales and an along-swath standard deviation of 4.38 cm. Although smaller than the mesoscale SSH signals associated with the KE variability, this SSH error amplitude is on par with the submesoscale SSH signals with spatial scales shorter than $O(30)$ km in the KE region [see Fig. 15 in Qiu et al. (2018)].

To reconstruct the upper-ocean w and ζ fields from the synthetic SWOT data, we first add the measurement errors shown in Fig. 10b to the along-swath SSH data of Fig. 10a. To minimize the measurement and sampling errors, we adopt the objective interpolation method to convert the along-swath SSH output field (i.e., the sum of Figs. 10a,b) to a regular grid SSH field. The objective interpolation formulation has an autocovariance function similar to Eq. (1) in time and in space with the temporal and spatial decorrelation scales set at $L_t = 1.2$ days and $L_s = 50$ km, respectively [more details about the objective interpolation method used in this study can be found in the appendix of Qiu et al. (2016)]. Figure 10d shows the

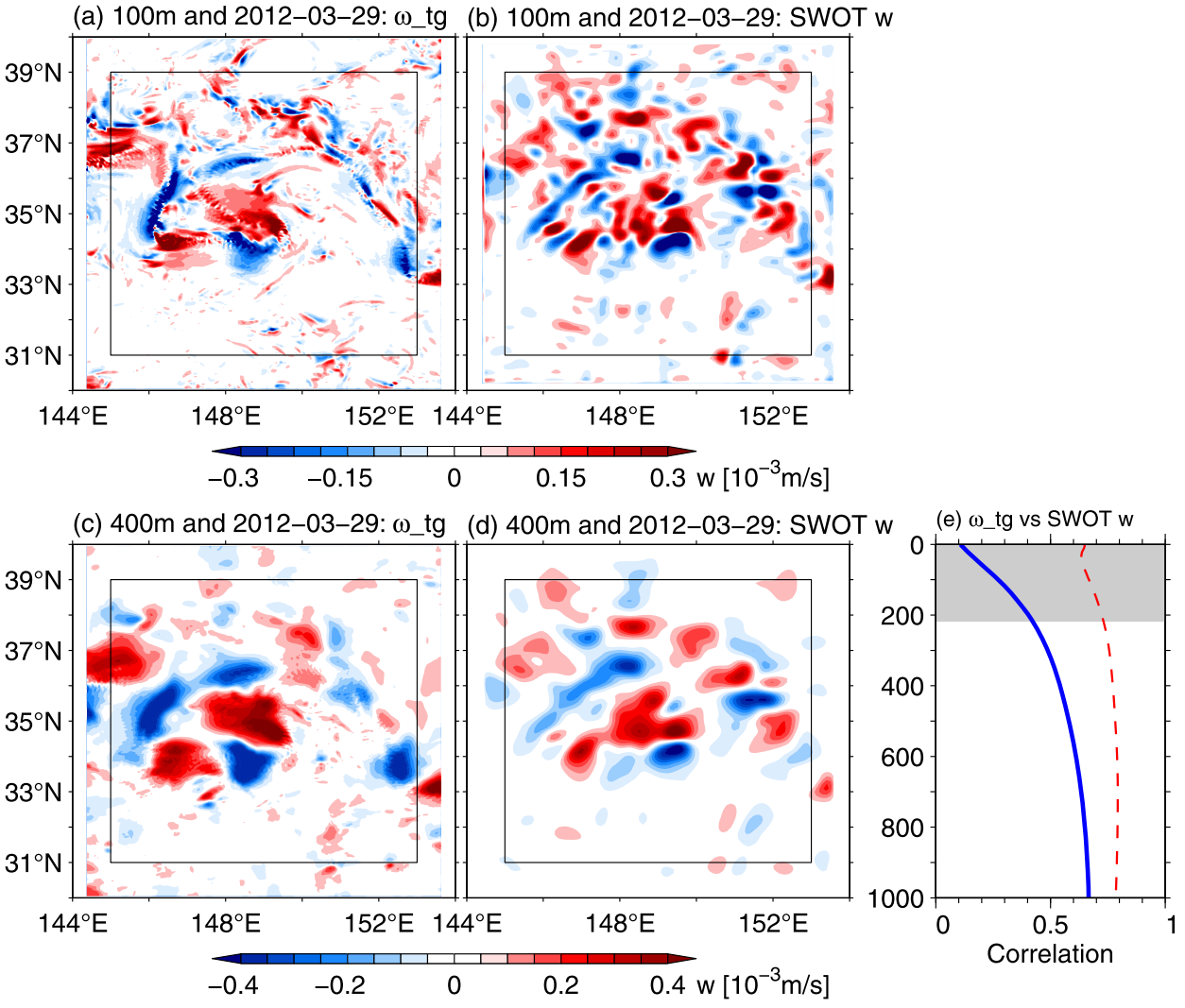

FIG. 11. Target w field at (a) 100- and (c) 400-m depth for the wintertime example centered on 29 Mar 2012. Reconstructed w field subject to the SWOT sampling and measurement errors at (b) 100- and (d) 400-m depth. (e) Correlation between the target and reconstructed w field with (solid line) and without (dashed line) the SWOT errors as a function of depth. Gray shading denotes the domain-averaged mixed layer depth.

objectively mapped SSH field on 29 March 2012 based on the SSH input of Figs. 10a and 10b. Compared to the original SSH field simulated by LLC4320 shown in Fig. 10c, it is clear that Fig. 10d captures most of the mesoscale features associated with the unstable KE jet. While their spatial correlation coefficient is high at 0.97, it is discernible that the objectively interpolated SSH map in Fig. 10d appears less spatially smoothed than the simulated SSH map of Fig. 10c due to the lack of full information about the rapidly evolving SSH signals and the addition of the SWOT measurement errors. A spectral analysis on the SSH maps reveals that Fig. 10d has more SSH variance in the 30–140-km wavelength range than that in Fig. 10c (figure not shown), implying that some of the internal tide and IGW signals are not fully removed in the objectively mapped SSH map.

Using this objectively mapped SSH field as input, we compare in Figs. 11a and 11b the target ω_{tg} field and the SWOT-based reconstructed w field at 100-m depth on 29 March 2012. In contrast to the reconstructed w result shown in Fig. 6b without the SWOT sampling and measurement errors, Fig. 11b exhibits more energetic signals with the 50–140-km scales relating to the increased SSH variance in this wavelength range in the input SSH field. In terms of the spatial correlation, there is a 0.37 reduction in correlation coefficient between Figs. 11a and 11b as compared to that between Figs. 6a and 6b (see Fig. 11e). A smaller reduction in spatial correlation

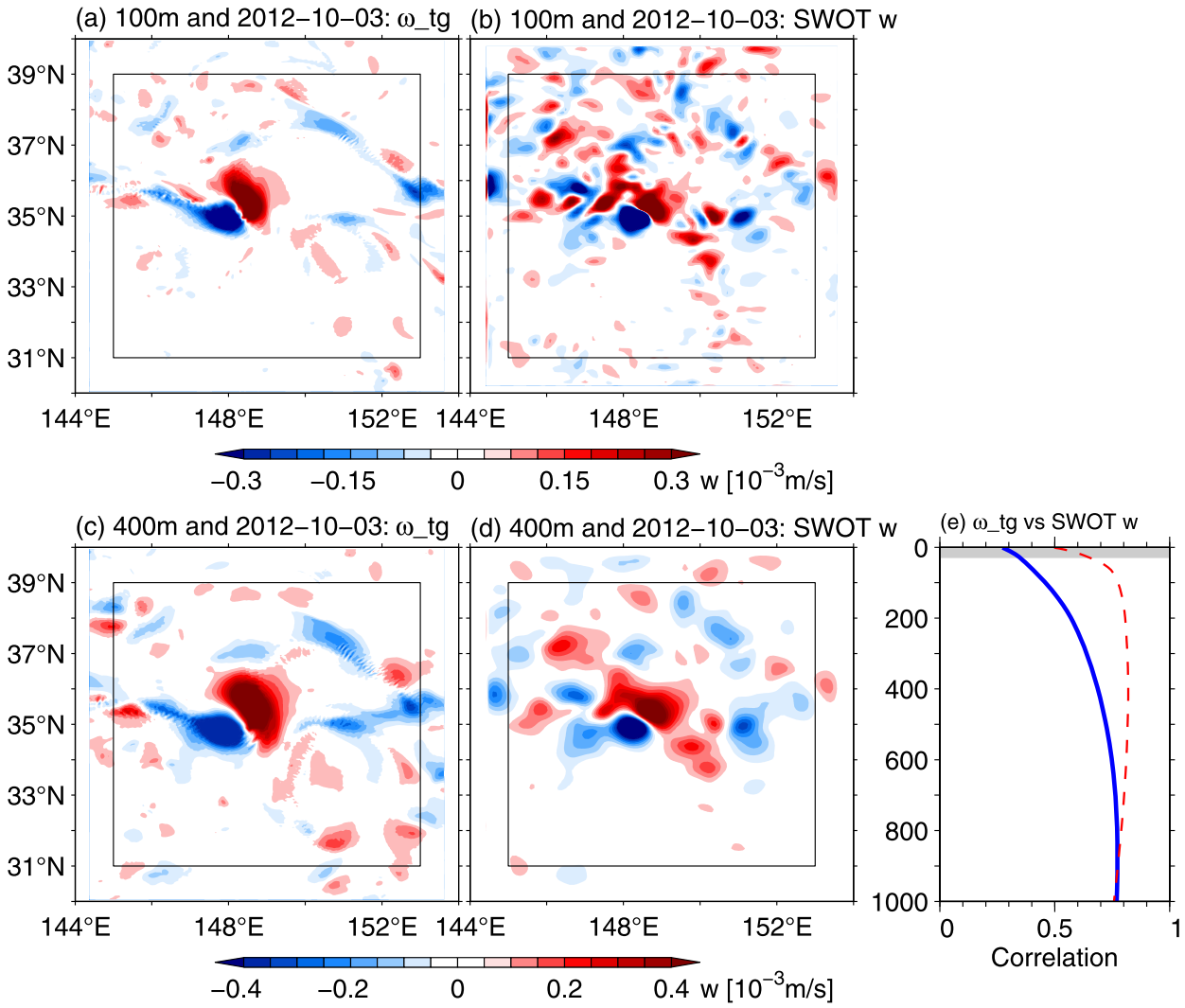

FIG. 12. Target w field at (a) 100- and (c) 400-m depth for the summertime example centered on 3 Oct 2012. Reconstructed w field subject to the SWOT sampling and measurement errors at (b) 100- and (d) 400-m depth. (e) Correlation between the target and reconstructed w field with (solid line) and without (dashed line) the SWOT errors as a function of depth. Gray shading denotes the domain-averaged mixed layer depth.

is found for the SWOT-based w reconstruction at the 400-m depth shown in Figs. 11c and 11d: instead of $r = 0.78$ in the case of error-free reconstruction, the spatial correlation between Figs. 11c and 11d is decreased to $r = 0.56$ when the SWOT sampling/measurement errors are taken into account.

The summer results for the SWOT-based w reconstruction are presented in Fig. 12. Compared to the winter example in Fig. 11, the reduction in spatial correlation due to the consideration of SWOT sampling/measurements errors has a smaller amplitude throughout the 1000-m upper ocean (Fig. 12e). This is the case because the summer vertical velocity signals are more dominated than in winter by signals with wavelengths greater than 150 km (cf. Fig. 12c). As such, they are less affected by the residual internal tide and IGW signals remaining in the objectively interpolated input SSH map.

Figure 13 shows the comparisons between the target and SWOT-based reconstructed surface ζ fields in winter (top row) and summer (bottom row), respectively. Like in the SWOT-based w reconstruction, spurious ζ signals with the 50–140-km wavelengths are apparent in Figs. 13b and 13e due to the residual internal tide and IGW signals remaining in the input SSH field. Compared to the results for w reconstruction, the reduction in spatial correlation between the ζ reconstruction with and without the SWOT sampling/measurement errors is smaller: the reduction is typically about 0.15 below the mixed layer

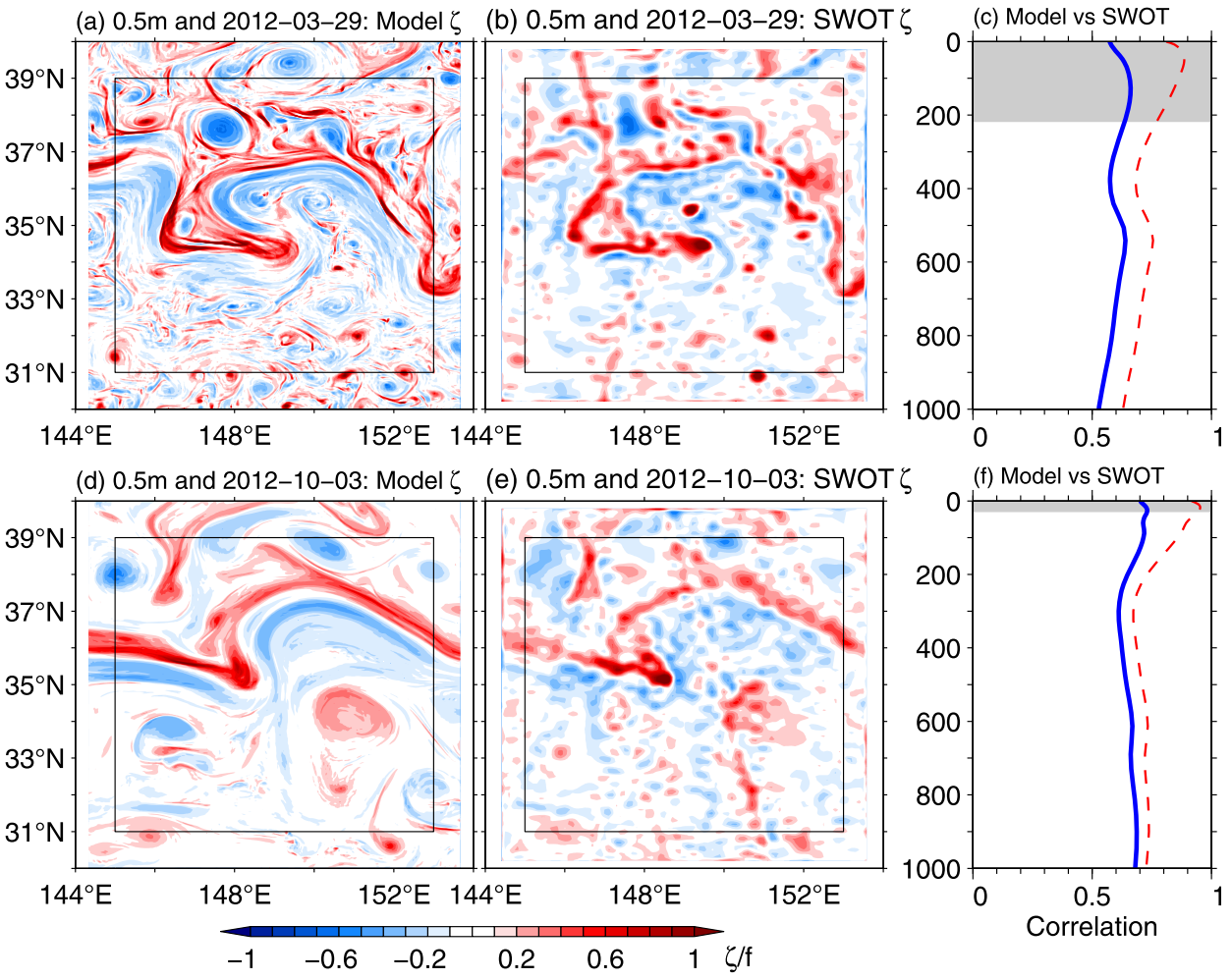

FIG. 13. (a) Target and (b) SWOT-reconstructed near-surface relative vorticity field for the wintertime example centered on 29 Mar 2012. (c) Correlation between the target and reconstructed ζ field with (solid line) and without (dashed line) the SWOT errors as a function of depth. (d),(e) As in (a)–(c), but for the summertime example centered on 3 Oct 2012. Gray shading in (c) and (f) denotes the domain-averaged mixed layer depth.

in winter and, in summer, the reduction reduces quickly from 0.2 near the surface to <0.08 below the 200-m depth.

In Fig. 14, we summarize the spatial correlations between the target and reconstructed w and ζ fields as a function of time and depth when the SWOT sampling/measurement errors are considered. As shown above by the winter and summer examples, the spatial correlation reduction in w reconstruction is generally larger than that for ζ (cf. blue and red curves in Figs. 14c,f). Below the mixed layer, the reconstructed vertical velocities have in general a spatial correlation with the target ω_{tw} field at r = 0.4–0.6. This coefficient value drops to below 0.3 within the mixed layer (Fig. 14a). For the reconstructed relative vorticity signals, their spatial correlation coefficient with the target ζ field stays around r = 0.6–0.7 throughout the 1000-m upper layer. The complex mixed layer dynamics in this case exerts no adverse impact upon the eSQG-based ζ reconstruction.

6. Summary and discussion

With the launch of the SWOT satellite scheduled for 2021, we have in this study explored the reconstructability of the 3D upper-ocean circulation structures with the use of synthetic SWOT SSH data. Specifically, our explorations utilized hourly output from the 1/48°-resolution MITgcm LLC4320 simulation that included realistic tidal forcing. When compared to our earlier study based on the daily output from the 1/30°-resolution OFES simulation without the tidal forcing (Qiu et al. 2016), the LLC4320 SSH field has a much improved representation of balanced versus unbalanced upper-ocean circulation

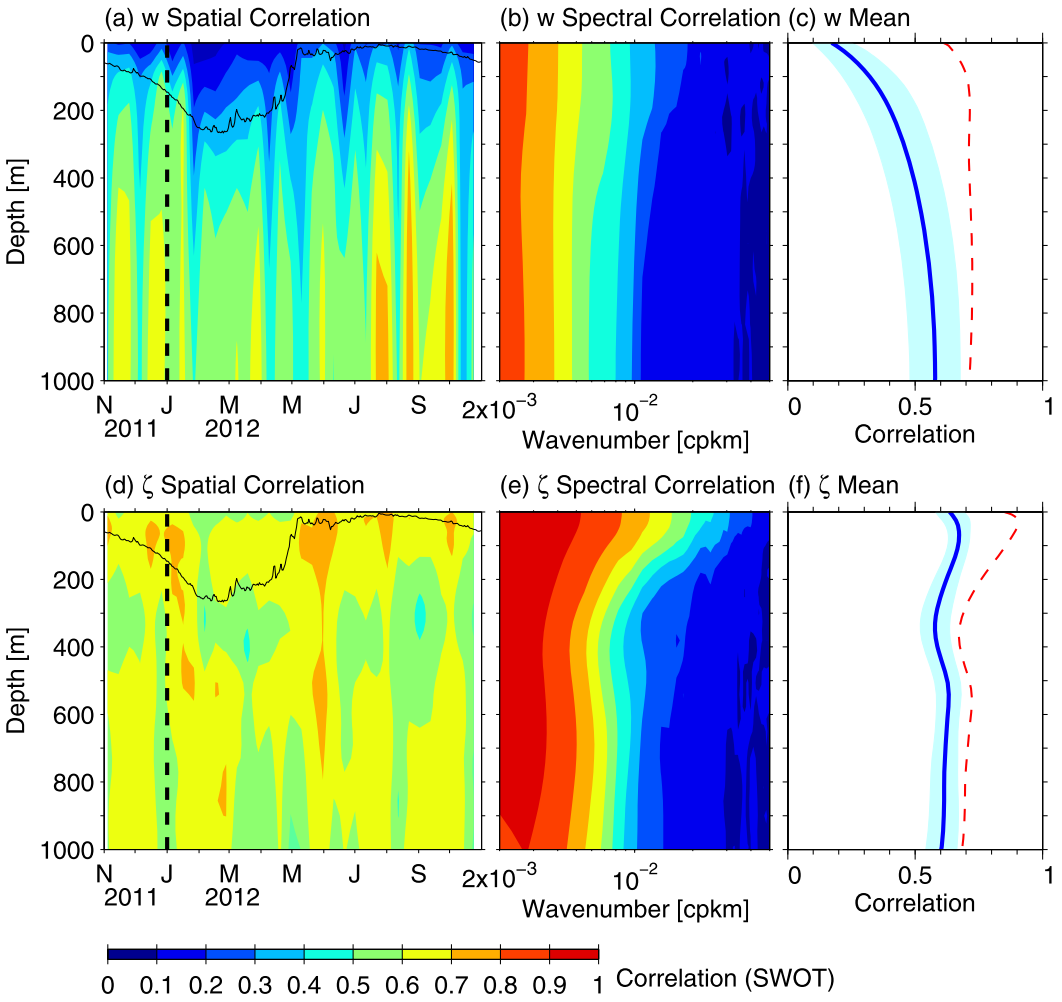

FIG. 14. (a) Correlation between the target and SWOT-reconstructed w field as a function of depth and time. The black line denotes the time series of the domain-averaged mixed layer depth. (b) The same correlation as a function of horizontal wavenumber. (c) Yearly averaged correlation between the target and reconstructed w field with (solid line) and without (dashed line) the SWOT errors as a function of depth. (d)–(f) As in (a)–(c), but for the correlation between the target and reconstructed ζ field.

and SSH variability in the World Ocean. In light of the good spatial, but poor temporal, sampling of the SWOT satellite, and given that the unbalanced internal tide and IGW motions can dominate the SSH signals in the wavelength range of $O(100)$ km or less, the use of hourly LLC4320 output to form the input SSH data for SWOT study is of paramount importance.

With the inclusion of external tidal forcing, the upper-ocean vertical circulation is significantly energized and it contains signals arising from diverse dynamical processes. Due to the constraint of spatial and temporal coverage of the SWOT measurement, we sought in this study the reconstruction of the upper-ocean circulation structures, including w, in the subinertial range. By decomposing the subinertial vertical velocity with use of the omega equation of the primitive equation system, we found that the majority of the w signals is determined by kinematic deformation of density anomalies by geostrophic horizontal motions below the surface mixed layer. Within the surface mixed layer, vertical mixing due to turbulent momentum/buoyancy fluxes and ageostrophic kinematic deformation can play an equally important role as that of the geostrophic kinematic deformation. Because the mixed layer depth undergoes a well-defined seasonal cycle, the vertical mixing and ageostrophic kinematic deformation effects are prominent in winter when the surface mixed layer is deep. For the vertical velocity reconstruction, we chose the w generated by the geostrophic kinematic deformation process to be our target field.

The theoretical framework for reconstruction adopted in this study is the effective SQG model put forth by Lapeyre and Klein (2006). The eSQG formalism

assumes the surface PV anomalies, inferable from the SSH data, are functionally related to the interior PV. Averaged over the 1-yr LLC4320 simulation period, the spatial correlation between the eSQG-reconstructed and target w field is $r = 0.7$ on average in the 100–1000-m layer. Within the surface mixed layer, the spatial correlation generally drops to $r < 0.6$ due to processes such as the vertical turbulent mixing. For the upper-ocean relative vorticity signals, the eSGQ reconstruction does a better job than for w and it shows no deterioration in spatial correlation relating to the surface mixed layer processes. The year-mean correlation between the simulated and reconstructed ζ field can reach up to $r > 0.85$ in the surface 100-m layer and it decreases to $r = 0.65$–0.75 below the 200-m depth.

To quantify how these idealized eSQG reconstructions are affected by the sampling and measurement errors intrinsic to the SWOT mission, we utilized the SWOT simulator to generate the synthetic SSH data along the SWOT descending and ascending swaths based on the hourly LLC4320 SSH data and the expected SWOT measurement errors. To reduce the sampling and measurement errors, we adopted an objective interpolation scheme and converted the irregularly sampled synthetic SSH data to a regular grid suitable for the eSQG reconstruction. Due to lack of full information about the spatiotemporally evolving balanced and unbalanced SSH signals from the discrete swath data, the sampling and measurement errors are found to negatively impact the w and ζ reconstructions. For the w signals beneath the surface mixed layer, the spatial correlation between the target and reconstructed w field exhibits drops from an averaged $r = 0.7$ in the idealized case to $r = 0.4$–0.6 in the SWOT case. The degradation in r is generally large in the upper layer, but tends to decrease with an increasing depth. This depth dependence is due to the fact that the SWOT sampling/measurement errors affect more on the submesoscale input SSH signals that are shallow reaching, than on the mesoscale signals that can extend deep into the interior ocean.

The degradation for ζ reconstruction due to the SWOT sampling/measurement errors has a similar depth dependence, but the magnitude of deterioration is in general smaller for ζ than w. The time-mean spatial correlation between the simulated and SWOT-reconstructed ζ field has $r = 0.6$–0.7 that shows little dependence on depth. The reason for a better reconstruction for ζ than for w is likely twofold. First, being a rotational component, relative vorticity is less impacted by unbalanced wave motions present in the synthetic SWOT SSH data than the vertical velocity. Second, compared to the ζ reconstruction, the w reconstruction in Eq. (7) involves not only the derivatives of the input SSH data once in z and twice in horizontal, but also the subtle phase changes between the SSH derivative and that of the density field.

Several improvements can be sought in future reconstruction effort relevant to the SWOT mission. While a proper framework for w reconstruction beneath the surface mixed layer, the eSQG formalism is inadequate for reconstructing w within the surface mixed layer. Several recent studies have attempted to address this deficiency by adding the downgradient turbulent mixing effect to the eSQG formulation (e.g., Ponte et al. 2013; Chavanne and Klein 2016). In this study, we have tried the vertical mixing parameterization scheme proposed by Ponte et al. (2013) and found no improvement in the w reconstruction inside the surface mixed layer (figures not shown). Rather than downgradient mixing of buoyancy, a recent study based on the LLC4320 simulation by Su et al. (2018) shows that the submesoscale turbulence within the surface mixed layer generates, in fact, upgradient buoyancy fluxes. Clearly, a better parameterization and understanding of the effect of turbulent momentum/buoyancy mixing in the mixed layer is called for.

For objective mapping, we adopted in this study a statistical approach to reduce the expected SWOT measurement errors and to convert the spatially and temporally irregular along-swath SSH data to a regular grid. This approach necessarily smears out the smaller scale SSH signals that are critical for finescale w and ζ reconstructions. An alternative approach to the objective mapping technique is to use a dynamical approach that takes into account nonlinear evolution of the mesoscale SSH field based on, for example, simplified shallow-water QG dynamics (Ubelmann et al. 2015) or primitive equation data assimilation (e.g., Li et al. 2019). By filling in the swath gaps dynamically, this approach preserves the fast-evolving, smaller-scale SSH features and can possibly lead to a better reconstruction for the smaller-scale w and ζ signals.

For future reconstruction studies, there is a need to minimize the internal tide and IGW signals present in the along-swath SSH data that is used as input for reconstruction. In our present study, the SSH signals associated with the unbalanced wave motions are aliased into the objectively mapped input SSH signals for reconstruction. Since the eSQG reconstruction is concerned with the balanced upper-ocean circulation structures, it will be highly beneficial to separate the balanced and unbalanced SSH signals in order to minimize the contamination by unbalanced SSH signals in the input SSH data. Finally, the Kuroshio Extension region considered in this study has energetic balanced motions. Reconstructability of the upper-ocean vertical velocity and relative vorticity field is unknown for regions with less balanced motions, such as near the SWOT calibration

site in the California Current. Further exploration of this site is underway.

Acknowledgments. We thank Rosemary Morrow, Clement Ubelmann and Guillaume Lapeyre for insightful discussions. Constructive comments made by two anonymous reviewers helped improve an early version of the manuscript. B.Q. and S.C. acknowledge support from NASA SWOT mission (NNX16AH66G). P.K. is supported by a NASA Senior Fellowship and by the SWOT project (JPL, NASA). J.W., H.T., L.F. and D.M's research presented in this paper was carried out in part at the Jet Propulsion Laboratory, California Institute of Technology, under contract with NASA. They acknowledge support from the SWOT projects.

APPENDIX A

Omega Equation in the Primitive Equation (PE) System

To obtain the ω equation within the PE framework, we follow in this study the notations put forth by Giordani et al. (2006). The PE horizontal momentum and density equations under the Boussinesq, hydrostatic, and *f*-plane approximations are

$$\frac{D\mathbf{u}}{Dt} + f\mathbf{k}\times\mathbf{u}_{\rm ag} = -\frac{1}{\rho_o}\frac{\partial \boldsymbol{\tau}_{x_i}}{\partial x_i}, \tag{A1}$$

$$\frac{D\rho}{Dt} = -\frac{\partial F_{x_i}}{\partial x_i}, \tag{A2}$$

where horizontal velocity $\mathbf{u} = \mathbf{u}_g + \mathbf{u}_{\rm ag}$ may be decomposed into its geostrophic and ageostrophic components, $\mathbf{k}$ is the vertical unit vector, f is the local Coriolis parameter, ρ is density, ρ_o is the reference density, $x_i = (x, y, z)$, $\boldsymbol{\tau}_{x_i}$ is the 3D turbulent momentum flux tensor, and F_{x_i} are the 3D turbulent buoyancy fluxes, respectively. The geostrophic velocity $\mathbf{u}_g$ is related to the density ρ via the thermal wind balance: $f\partial\mathbf{u}_g/\partial z = -(g/\rho_o)\mathbf{k}\times\nabla_h\rho$. In this PE system, the mass conservation equation can be written as

$$\nabla_h\cdot\mathbf{u}_{\rm ag} + \frac{\partial w}{\partial z} = 0, \tag{A3}$$

where ∇_h is the horizontal gradient operator.

By taking $\partial[\mathbf{k}\cdot\nabla_h\times$ (A1)$]/\partial z - \nabla_h\cdot[\nabla_h$(A2)$]$ and combining with Eq. (A3), we obtain the PE ω equation in the following generalized **Q**-vector formulation:

$$f^2\frac{\partial^2\omega}{\partial z^2} + \nabla_h(N^2\cdot\nabla_h\omega) = \nabla_h\cdot\mathbf{Q}, \tag{A4}$$

where $N^2 = -(g/\rho_0)\partial\rho/\partial z$ is squared buoyancy frequency and $\mathbf{Q}$ is a horizontal vector composed of

$$\mathbf{Q} = \mathbf{Q}_{\rm th} + \mathbf{Q}_{\rm dm} + \mathbf{Q}_{\rm tg} + \mathbf{Q}_{\rm tag} + \mathbf{Q}_{\rm dag} + \mathbf{Q}_{\rm dr}. \tag{A5}$$

In Eq. (A5),

$$\mathbf{Q}_{\rm th} = -\frac{g}{\rho_0}\nabla_h\left(\frac{\partial F_{x_i}}{\partial x_i}\right) \tag{A6}$$

denotes the forcing by turbulent buoyancy fluxes, and

$$\mathbf{Q}_{\rm dm} = -\frac{f}{\rho_0}\frac{\partial}{\partial z}\left(\mathbf{k}\times\frac{\partial\boldsymbol{\tau}_{x_i}}{\partial x_i}\right) \tag{A7}$$

denotes the forcing by turbulent momentum fluxes.

In contrast to the above turbulent mixing forcings, the remaining four vectors in Eq. (A5) represent dynamic forcing. Specifically,

$$\mathbf{Q}_{\rm tg} = \frac{2g}{\rho_0}(\nabla_h\mathbf{u}_g)^{\rm T}\cdot\nabla_h\rho \tag{A8}$$

denotes the kinematic deformation caused by the geostrophic horizontal flow and is known as the QG **Q** vector, or the frontogenesis vector (Hoskins et al. 1978). Similarly,

$$\mathbf{Q}_{\rm tag} = \frac{2g}{\rho_0}(\nabla_h\mathbf{u}_{\rm ag})^{\rm T}\cdot\nabla_h\rho \tag{A9}$$

denotes the kinematic deformation caused by the ageostrophic horizontal flow. In Eq. (A5), $\mathbf{Q}_{\rm dag}$ denotes deformation caused by the thermal wind imbalance $f\partial\mathbf{u}_{\rm ag}/\partial z$:

$$\mathbf{Q}_{\rm dag} = -f[\nabla_h(\mathbf{k}\times\mathbf{u})]^{\rm T}\cdot\frac{\partial\mathbf{u}_{\rm ag}}{\partial z}. \tag{A10}$$

As noted in Giordani et al. (2006), the $\mathbf{Q}_{\rm dag}$ forcing represents the stretching and reorientation by the total $\mathbf{u}$ field of the preexisting ageostrophic horizontal pseudovorticity. Last, $\mathbf{Q}_{\rm dr}$ in Eq. (A5) denotes the forcing by the material derivative of the thermal wind imbalance and is given by

$$\mathbf{Q}_{\rm dr} = -f\mathbf{k}\times\frac{D}{Dt}\left(\frac{\partial\mathbf{u}_{\rm ag}}{\partial z}\right). \tag{A11}$$

To solve ω based on Eq. (A4), we first use the hourly output of LLC4320 to evaluate $\mathbf{Q}_{\rm tg}$, $\mathbf{Q}_{\rm tag}$, $\mathbf{Q}_{\rm dag}$ and $\mathbf{Q}_{\rm dr}$ according to Eqs. (A8)–(A11) in the 10° × 10° KE box of 30°–40°N and 144°–154°E. After calculating $\nabla_h\cdot\mathbf{Q}$, we remove its large-scale signals through the bilinear

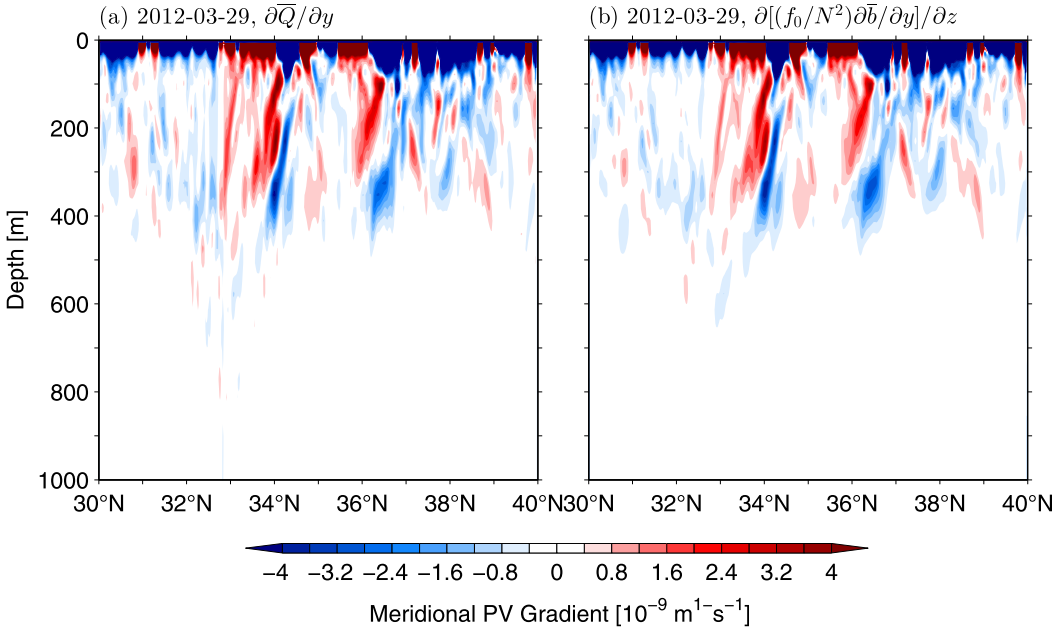

FIG. B1. (a) Mean PV gradient $\partial\overline{Q}/\partial y$ profiles on 29 Mar in the LLC4320 simulation. Here, the zonal average is taken from 144° to 154°E. (b) As in (a), but for mean PV gradient due to vortex stretching: $\partial[(f_0/N^2)\partial\overline{b}/\partial y]/\partial z$.

least-squared fitting, and periodize the $\nabla_h \cdot \mathbf{Q}$ field by doubling the $10° \times 10°$ box using mirror symmetry in the x and y directions. By Fourier transforming $w(x, y, z)$, we then obtain $\hat{\omega}(k_x, k_y, z)$. For each pair of horizontal wavenumbers k_x and k_y, $\hat{\omega}(k_x, k_y, z)$ is solved numerically based on discretized Eq. (A4) using centered differencing in the z direction and using the boundary conditions $\hat{\omega} = 0$ at $z = 0$ and $\partial\hat{\omega}/\partial z = 0$ at $z = 1000$ m. Once $\hat{\omega}(k_x, k_y, z)$ is determined, $\omega(x, y, z)$ is obtained via inverse Fourier transform.

APPENDIX B

The Effective SQG Framework in the LLC4320 Simulation

Two important assumptions are adopted by Lapeyre and Klein (2006) in their development of the eSQG model. The first assumption is that the large-scale meridional PV gradient:

$$\frac{\partial\overline{Q}}{\partial y} = \beta - \frac{\partial^2\overline{u}}{\partial y^2} + \frac{1}{f_0}\frac{\partial}{\partial z}\left(\frac{f_0^2}{N^2}\frac{\partial\overline{b}}{\partial y}\right), \tag{B1}$$

where an overbar denotes the zonal average, is largely determined by the vortex stretching term, that is, the last term in Eq. (B1). To test this assumption, we plot in Fig. B1a $\partial\overline{Q}/\partial y$ versus $\partial[(f_0/N^2)\partial\overline{b}/\partial y]/\partial z$ in Fig. B1b as a function of y and z based on the LLC4320 output on 29 March 2012, the winter example date shown in Fig. 1. The two patterns show a very good match, indicating that it is the stretching term that dominates the mean PV gradient. Results similar to Fig. B1 are obtained for other dates of the LLC4320 output.

The second assumption underlying the eSQG formalism is that the proportionality $\alpha(z)$ between the mean PV gradient and the mean buoyancy gradient at the surface:

$$\frac{\partial\overline{Q}}{\partial y} \approx \frac{1}{f_0}\alpha(z)\frac{\partial\overline{b_s}}{\partial y} \tag{B2}$$

is functionally similar to that between the PV anomalies and the surface buoyancy anomalies:

$$Q'(x, y, z) \approx \frac{1}{f_0}\alpha(z)b_s'(x, y). \tag{B3}$$

Validity of Eq. (B3) implies that the interior PV anomalies are governed by the surface buoyancy anomalies and the Q'-induced interior perturbation streamfunction solution has the same phase as the b_s'-induced surface perturbation streamfunction solution (Lapeyre and Klein 2006). In Fig. B2, we plot the time series of $\alpha(z)$ based on regression of $\partial\overline{Q}/\partial y$ (Fig. B2a) against $\partial\overline{b_s}/\partial y$ and regression of Q' against b_s' (Fig. B2b). The good agreement between the two $\alpha(z)$ profiles at all depths and times

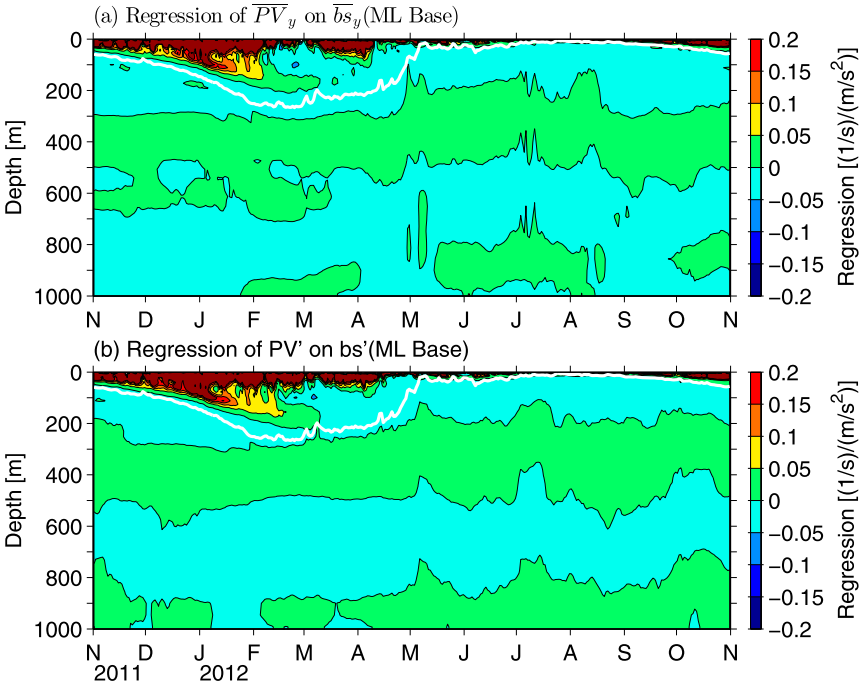

FIG. B2. (a) Time series of $\alpha(z)$ based on regression of $\partial\overline{Q}/\partial y$ against $\partial\overline{b}_s/\partial y$ [cf. Eq. (B2)] in the KE box of 30°–40°N and 144°–154°E. (b) Time series of $\alpha(z)$ based on regression of Q' against b_s' [cf. Eq. (B3)]. The two $\alpha(z)$ profiles have a correlation coefficient $r = 0.88$.

indicates that the second assumption for the eSQG formalism is also valid in the LLC4320 output in the KE region of our interest.

REFERENCES

Arbic, B., and Coauthors, 2018: A primer on global internal tide and internal gravity wave continuum modeling in HYCOM and MITgcm. *New Frontiers in Operational Oceanography*, E. P. Chassignet et al., Eds., GODAE Ocean View, 307–392, https://doi.org/10.17125/gov2018.ch13.

Blumen, W., 1978: Uniform potential vorticity flow: Part I. Theory of wave interactions and two-dimensional turbulence. *J. Atmos. Sci.*, **35**, 774–783, https://doi.org/10.1175/1520-0469(1978)035<0774:UPVFPI>2.0.CO;2.

Callies, J., and W. Wu, 2019: Some expectations for submesoscale sea surface height spectra. *J. Phys. Oceanogr.*, **49**, 2271–2289, https://doi.org/10.1175/JPO-D-18-0272.1.

——, R. Ferrari, J. M. Klymak, and J. Gula, 2015: Seasonality in submesoscale turbulence. *Nat. Commun.*, **6**, 6862, https://doi.org/10.1038/ncomms7862.

Chavanne, C. P., and P. Klein, 2016: Quasigeostrophic diagnosis of mixed layer dynamics embedded in a mesoscale turbulent field. *J. Phys. Oceanogr.*, **46**, 275–287, https://doi.org/10.1175/JPO-D-14-0178.1.

Chelton, D. B., M. G. Schlax, and R. M. Samelson, 2011: Global observations of nonlinear mesoscale eddies. *Prog. Oceanogr.*, **91**, 167–216, https://doi.org/10.1016/j.pocean.2011.01.002.

Dong, C., J. C. McWilliams, Y. Liu, and D. Chen, 2014: Global heat and salt transports by eddy movement. *Nat. Commun.*, **5**, 3294, https://doi.org/10.1038/ncomms4294.

Ferrari, R., and C. Wunsch, 2009: Ocean circulation kinetic energy: Reservoirs, sources, and sinks. *Annu. Rev. Fluid Mech.*, **41**, 253–282, https://doi.org/10.1146/annurev.fluid.40.111406.102139.

Fu, L.-L., and C. Ubelmann, 2014: On the transition from profile altimetry to swath altimeter for observing global ocean surface topography. *J. Atmos. Oceanic Technol.*, **31**, 560–568, https://doi.org/10.1175/JTECH-D-13-00109.1.

——, D. B. Chelton, P.-Y. Le Traon, and R. Morrow, 2010: Eddy dynamics from satellite altimetry. *Oceanography*, **23**, 14–25, https://doi.org/10.5670/oceanog.2010.02.

Gaultier, L., C. Ubelmann, and L.-L. Fu, 2016: The challenge of using future SWOT data for oceanic field reconstruction. *J. Atmos. Oceanic Technol.*, **33**, 119–126, https://doi.org/10.1175/JTECH-D-15-0160.1.

Gill, A. E., 1982: *Atmosphere-Ocean Dynamics*. International Geophysics Series, Vol. 30, Academic Press, 662 pp.

Giordani, H., L. Prieur, and G. Caniaux, 2006: Advanced insights into sources of vertical velocity in the ocean. *Ocean Dyn.*, **56**, 513–524, https://doi.org/10.1007/s10236-005-0050-1.

Gonzalez-Haro, C., and J. Isern-Fontanet, 2014: Global ocean current reconstruction from altimetric and microwave SST measurements. *J. Geophys. Res. Oceans*, **119**, 3378–3391, https://doi.org/10.1002/2013JC009728.

Held, I. M., R. T. Pierrehumbert, S. T. Garner, and K. L. Swanson, 1995: Surface quasi-geostrophic dynamics. *J. Fluid Mech.*, **282**, 1–20, https://doi.org/10.1017/S0022112095000012.

Hoskins, B. J., I. Draghichi, and H. C. Davies, 1978: A new look at the ω-equation. *Quart. J. Roy. Meteor. Soc.*, **104**, 31–38, https://doi.org/10.1002/qj.49710443903.

Imawaki, S., A. S. Bower, L. Beal, and B. Qiu, 2013: Western boundary currents. *Ocean Circulation and Climate - A 21st Century Perspective*, 2nd ed. G. Siedler et al., Eds., Academic Press, 305–338.

Isern-Fontanet, J., and E. Hascoët, 2014: Diagnosis of high-resolution upper ocean dynamics from noisy sea surface temperatures. *J. Geophys. Res. Oceans*, **119**, 121–132, https://doi.org/10.1002/2013JC009176.

——, J. B. Chapron, P. Klein, and G. Lapeyre, 2006: Potential use of microwave sea surface temperatures for the estimation of ocean currents. *Geophys. Res. Lett.*, **33**, L24608, https://doi.org/10.1029/2006GL027801.

——, G. Lapeyre, P. Klein, B. Chapron, and M. Hecht, 2008: Three dimensional reconstruction of oceanic mesoscale currents from surface information. *J. Geophys. Res.*, **113**, C09005, https://doi.org/10.1029/2007JC004692.

Klein, P., and G. Lapeyre, 2009: The oceanic vertical pump induced by mesoscale and submesoscale turbulence. *Annu. Rev. Mar. Sci.*, **1**, 351–375, https://doi.org/10.1146/annurev.marine.010908.163704.

——, J. Isern-Fontanet, G. Lapeyre, G. Roullet, E. Danioux, B. Chapron, S. Le Gentil, and H. Sasaki, 2009: Diagnosis of vertical velocities in the upper ocean from high resolution sea surface height. *Geophys. Res. Lett.*, **36**, L12603, https://doi.org/10.1029/2009GL038359.

LaCasce, J., and A. Mahadevan, 2006: Estimating subsurface horizontal and vertical veloci-ties from sea surface temperature. *J. Mar. Res.*, **64**, 695–721, https://doi.org/10.1357/002224006779367267.

Lapeyre, G., and P. Klein, 2006: Dynamics of the upper oceanic layers in terms of surface quasigeostrophy theory. *J. Phys. Oceanogr.*, **36**, 165–176, https://doi.org/10.1175/JPO2840.1.

Lévy, R., R. Ferrari, P. J. S. Franks, A. P. Martin, and P. Rivière, 2012: Bringing physics to life at the submesoscale. *Geophys. Res. Lett.*, **39**, L14602, https://doi.org/10.1029/2012GL052756.

Li, Z., J. Wang, and L.-L. Fu, 2019: An observing system simulation experiment for ocean state estimation to assess the performance of the SWOT mission: Part 1—A twin experiment. *J. Geophys. Res. Oceans*, **124**, 4838–4855, https://doi.org/10.1029/2018JC014869.

Mahadevan, A., 2016: The impact of submesoscale physics on primary productivity of plankton. *Annu. Rev. Mar. Sci.*, **8**, 161–184, https://doi.org/10.1146/annurev-marine-010814-015912.

Marshall, J. C., A. Adcroft, C. Hill, L. Perelman, and C. Heisey, 1997: A finite-volume, incompressible Navier Stokes model for studies of the ocean on parallel computers. *J. Geophys. Res.*, **102**, 5753–5766, https://doi.org/10.1029/96JC02775.

McGillicuddy, D. J., Jr., 2016: Mechanisms of physical-biological-biogeochemical interaction at the oceanic mesoscale. *Annu. Rev. Mar. Sci.*, **8**, 125–159, https://doi.org/10.1146/annurev-marine-010814-015606.

McWilliams, J. C., 2016: Submesoscale currents in the ocean. *Proc. Roy. Soc. London*, **472A**, 20160117, https://doi.org/10.1098/rspa.2016.0117.

Menemenlis, D., and Coauthors, 2008: ECCO2: High-resolution global ocean and sea ice data synthesis. Mercator Ocean Quarterly Newsletter, No. 31, Mercator Ocean, Ramonville Saint-Agne, France, 13–21, https://www.mercator-ocean.fr/wp-content/uploads/2015/06/lettre_31_en.pdf.

Mensa, J. A., Z. Garraffo, A. Griffa, T. M. Ozgokmen, A. Haza, and M. Veneziani, 2013: Seasonality of the submesoscale dynamics in the Gulf Stream region. *Ocean Dyn.*, **63**, 923–941, https://doi.org/10.1007/s10236-013-0633-1.

Morrow, R., L.-L. Fu, J. T. Farrar, H. Seo, and P.-Y. Le Traon, 2017: Ocean eddies and mesoscale variability. *Satellite Altimetry over Oceans and Land Surfaces*, D. Stammer and A. Cazenava, Eds., CRC Press, 315–342.

Nagai, T., A. Tandon, and D. L. Rudnick, 2006: Two-dimensional ageostrophic secondary circulation at ocean fronts due to vertical mixing and large-scale deformation. *J. Geophys. Res.*, **111**, C09038, https://doi.org/10.1029/2005JC002964.

Pallàs-Sanz, E., and A. Viúdez, 2005: Diagnozing mesoscale vertical motion from horizontal velocity and density data. *J. Phys. Oceanogr.*, **35**, 1744–1762, https://doi.org/10.1175/JPO2784.1.

Pascual, A., S. Ruiz, B. Buongiorno Nardelli, S. Guinehut, D. Iudicone, and J. Tintoré, 2015: Net primary production in the Gulf Stream sustained by quasi-geostrophic vertical exchanges. *Geophys. Res. Lett.*, **42**, 441–449, https://doi.org/10.1002/2014GL062569.

Pollard, R. T., and L. A. Regier, 1992: Vorticity and vertical circulation at an ocean front. *J. Phys. Oceanogr.*, **22**, 609–625, https://doi.org/10.1175/1520-0485(1992)022<0609:VAVCAA>2.0.CO;2.

Ponte, A. L., and P. Klein, 2013: Reconstruction of the upper ocean 3D dynamics from high-resolution sea surface height. *Ocean Dyn.*, **63**, 777–791, https://doi.org/10.1007/s10236-013-0611-7.

——, ——, X. Capet, P.-Y. Le Traon, B. Chapron, and P. Lherminier, 2013: Diagnosing surface mixed layer dynamics from high-resolution satellite observations: Numerical insights. *J. Phys. Oceanogr.*, **43**, 1345–1355, https://doi.org/10.1175/JPO-D-12-0136.1.

Qiu, B., S. Chen, P. Klein, H. Sasaki, and Y. Sasai, 2014: Seasonal mesoscale and submesoscale eddy variability along the North Pacific Subtropical Countercurrent. *J. Phys. Oceanogr.*, **44**, 3079–3098, https://doi.org/10.1175/JPO-D-14-0071.1.

——, ——, ——, C. Ubelmann, L.-L. Fu, and H. Sasaki, 2016: Reconstructability of three-dimensional upper-ocean circulation from SWOT sea surface height measurements. *J. Phys. Oceanogr.*, **46**, 947–963, https://doi.org/10.1175/JPO-D-15-0188.1.

——, T. Nakano, S. Chen, and P. Klein, 2017: Submesoscale transition from geostrophic flows to internal waves in the northwestern Pacific upper ocean. *Nat. Commun.*, **8**, 14055, https://doi.org/10.1038/ncomms14055.

——, S. Chen, P. Klein, J. Wang, H. Torres, L.-L. Fu, and D. Menemenlis, 2018: Seasonality in transition scale from balanced to unbalanced motions in the world ocean. *J. Phys. Oceanogr.*, **48**, 591–605, https://doi.org/10.1175/JPO-D-17-0169.1.

Rocha, C. B., T. K. Chereskin, S. T. Gille, and D. Menemenlis, 2016a: Mesoscale to submesoscale wavenumber spectra in Drake Passage. *J. Phys. Oceanogr.*, **46**, 601–620, https://doi.org/10.1175/JPO-D-15-0087.1.

——, S. T. Gille, T. K. Chereskin, and D. Menemenlis, 2016b: Seasonality of submesoscale dynamics in the Kuroshio Extension. *Geophys. Res. Lett.*, **43**, 11 304–11 311, https://doi.org/10.1002/2016GL071349.

Rudnick, D. L., 1996: Intensive surveys of the Azores front: 2. Inferring the geostrophic and vertical velocity fields. *J. Geophys. Res.*, **101**, 16 291–16 303, https://doi.org/10.1029/96JC01144.

Sasaki, H., P. Klein, B. Qiu, and Y. Sasai, 2014: Impact of oceanic-scale interactions on the seasonal modulation of ocean dynamics by the atmosphere. *Nat. Commun.*, **5**, 5636, https://doi.org/10.1038/ncomms6636.

Savage, A. C., and Coauthors, 2017a: Frequency content of sea surface height variability from internal gravity waves to mesoscale eddies. *J. Geophys. Res. Oceans*, **122**, 2519–2538, https://doi.org/10.1002/2016JC012331.

——, and Coauthors, 2017b: Spectral decomposition of internal gravity wave sea surface height in global models. *J. Geophys. Res.*, **122**, 7803–7821, https://doi.org/10.1002/2017JC013009.

Smith, K. S., and J. Vanneste, 2013: A surface-aware projection basis for quasigeostrophic flow. *J. Phys. Oceanogr.*, **43**, 548–562, https://doi.org/10.1175/JPO-D-12-0107.1.

Su, Z., J. Wang, P. Klein, A. F. Thompson, and D. Menemenlis, 2018: Ocean submesoscales as a key component of the global heat budget. *Nat. Commun.*, **9**, 775, https://doi.org/10.1038/s41467-018-02983-w.

Torres, H. S., P. Klein, D. Menemenlis, B. Qiu, Z. Su, J. Wang, S. Chen, and L.-L. Fu, 2018: Partitioning ocean motions into balanced motions and internal gravity waves: A modeling study in anticipation of future space missions. *J. Geophys. Res. Oceans*, **123**, 8084–8105, https://doi.org/10.1029/2018JC014438.

Ubelmann, C., P. Klein, and L.-L. Fu, 2015: Dynamic interpolation of sea surface height and potential applications for future high-resolution altimetry mapping. *J. Atmos. Oceanic Technol.*, **32**, 177–184, https://doi.org/10.1175/JTECH-D-14-00152.1.

Wang, J., G. R. Flierl, J. H. LaCasce, J. L. McClean, and A. Mahadevan, 2013: Reconstructing the ocean's interior from surface data. *J. Phys. Oceanogr.*, **43**, 1611–1626, https://doi.org/10.1175/JPO-D-12-0204.1.

——, L.-L. Fu, B. Qiu, D. Menemenlis, J. T. Farrar, Y. Chao, A. F. Thompson, and M. M. Flexas, 2018: An observing system simulation experiment for the calibration and validation of the Surface Water Ocean Topography sea surface height measurement using in situ platforms. *J. Atmos. Oceanic Technol.*, **35**, 281–297, https://doi.org/10.1175/JTECH-D-17-0076.1.

——, ——, H. Torres, S. Chen, B. Qiu, and D. Menemenlis, 2019: On the spatial scales to be resolved by the Surface Water and Ocean Topography Ka-band radar interferometer. *J. Atmos. Oceanic Technol.*, **36**, 87–99, https://doi.org/10.1175/JTECH-D-18-0119.1.

Weis, P., M. Thomas, and J. Sündermann, 2008: Broad frequency tidal dynamics simulated by a high-resolution global ocean tide model forced by ephemerides. *J. Geophys. Res.*, **113**, C10029, https://doi.org/10.1029/2007JC004556.

Zhang, Z., W. Wang, and B. Qiu, 2014: Oceanic mass transport by mesoscale eddies. *Science*, **345**, 322–324, https://doi.org/10.1126/science.1252418.